This is the accepted manuscript made available via CHORUS. The article has been published as:

Total absorption spectroscopy of the math xmlns="http://www.w3.org/1998/Math/MathML">mi>β/mi> /math> decay of math xmlns="http://www.w3.org/1998/Math/MathML">mmultiscripts>mi>Zr/mi>mprescripts>/mprescripts>none>/none>mrow>mn>101/mn>mo>,/mo>mn>102/mn>/mrow>/mmultiscripts>/math> and math xmlns="http://www.w3.org/1998/Math/MathML">mmultiscripts>mi>Tc/mi>mprescripts>/mprescripts>none>/none>mn>109/mn>/mmultiscripts>/math>

A. C. Dombos, A. Spyrou, F. Naqvi, S. J. Quinn, S. N. Liddick, A. Algora, T. Baumann, J. Brett, B. P. Crider, P. A. DeYoung, T. Ginter, J. Gombas, S. Lyons, T. Marketin, P. Möller, W.-J. Ong, A. Palmisano, J. Pereira, C. J. Prokop, P. Sarriguren, D. P. Scriven, A. Simon, M. K. Smith, and S. Valenta

Phys. Rev. C **103**, 025810 — Published 25 February 2021

DOI: 10.1103/PhysRevC.103.025810

Total absorption spectroscopy of the β decay of ^{101,102}Zr and ^{109}Tc

A. C. Dombos,[1,2,3,*] A. Spyrou,[1,2,3] F. Naqvi,[1,3] S. J. Quinn,[1,2,3] S. N. Liddick,[1,4,3] A. Algora,[5,6] T. Baumann,[1] J. Brett,[7] B. P. Crider,[1,8] P. A. DeYoung,[7] T. Ginter,[1] J. Gombas,[7] S. Lyons,[1,3,†] T. Marketin,[9] P. Möller,[10,‡] W.-J. Ong,[1,2,3] A. Palmisano,[1,2,3] J. Pereira,[1,3] C. J. Prokop,[1,4] P. Sarriguren,[11] D. P. Scriven,[2] A. Simon,[12] M. K. Smith,[1,3] and S. Valenta[13]

[1]*National Superconducting Cyclotron Laboratory, Michigan State University, East Lansing, Michigan 48824, USA*
[2]*Department of Physics and Astronomy, Michigan State University, East Lansing, Michigan 48824, USA*
[3]*Joint Institute for Nuclear Astrophysics, Michigan State University, East Lansing, Michigan 48824, USA*
[4]*Department of Chemistry, Michigan State University, East Lansing, Michigan 48824, USA*
[5]*Instituto de Física Corpuscular, CSIC-Universidad de Valencia, E-46071, Valencia, Spain*
[6]*Institute of Nuclear Research of the Hungarian Academy of Sciences, Debrecen H-4026, Hungary*
[7]*Department of Physics, Hope College, Holland, Michigan 49422-9000, USA*
[8]*Department of Physics and Astronomy, Mississippi State University, Mississippi State, Mississippi 39762, USA*
[9]*Department of Physics, Faculty of Science, University of Zagreb, 10000 Zagreb, Croatia*
[10]*Theoretical Division, Los Alamos National Laboratory, Los Alamos, New Mexico 87545, USA*
[11]*Instituto Estructura de la Materia, IEM-CSIC, Serrano 123, E-28006 Madrid, Spain*
[12]*Department of Physics and Joint Institute for Nuclear Astrophysics, University of Notre Dame, Notre Dame, Indiana 46556, USA*
[13]*Faculty of Mathematics and Physics, Charles University, 180 00 Prague, Czech Republic*

The β decay of ^{101,102}Zr and ^{109}Tc was studied using the technique of total absorption spectroscopy. The experiment was performed at the National Superconducting Cyclotron Laboratory using the Summing NaI(Tl) (SuN) detector in the first-ever application of total absorption spectroscopy with a fast beam produced via projectile fragmentation. The β-decay feeding intensity and Gamow-Teller transition strength distributions were extracted for these three decays. The extracted distributions were compared to three different quasiparticle random-phase approximation (QRPA) models based on different mean-field potentials. A comparison with calculations from one of the QRPA models was performed to learn about the ground-state shape of the parent nucleus. For ^{101}Zr and ^{102}Zr, calculations assuming a pure shape configuration (oblate or prolate) were not able to reproduce the extracted distributions. These results may indicate that some type of mixture between oblate and prolate shapes is necessary to reproduce the extracted distributions. For ^{109}Tc, a comparison of the extracted distributions with QRPA calculations suggests a dominant oblate configuration. The other two QRPA models are commonly used to provide β-decay properties in r-process network calculations. This work shows the importance of making comparisons between the experimental and theoretical β-decay distributions, rather than just half-lives and β-delayed neutron emission probabilities, as close to the r-process path as possible.

I. INTRODUCTION

The rapid neutron-capture process, or r process, is the mechanism cited to explain the abundance of roughly half of the stable nuclides beyond the iron peak that are observed in the solar system [1]. Now that the r process has been observed to occur in the merger of two neutron stars [2], improving the accuracy of calculated nuclear physics quantities is necessary for r-process network calculations to reproduce the observed abundance pattern [3] and interpret the plethora of observational data offered by GW170817 and AT2017gfo [4]. In this case, the calculated nuclear physics quantities are the relevant nuclear physics properties of nuclides that participate in the r process. The nuclear physics properties include masses, fission properties, neutron capture cross sections, and β-decay properties. More specifically, the β-decay properties are the β-decay half-life ($T_{1/2}$) and β-delayed neutron emission probability (P_n).

Theoretical models are relied upon to provide β-decay properties ($T_{1/2}$ and P_n) for the thousands of nuclides in r-process network calculations that are not yet accessible by experiment. Therefore, the provided β-decay properties should be as accurate as possible. Usually, the accuracy of a theoretical model is evaluated by comparing its predictions of $T_{1/2}$ and P_n with experimental measurements of those quantities. However, $T_{1/2}$ and P_n are "integral quantities" or "integral properties." That is, they are single numbers that are obtained from a summation of the Gamow-Teller transition strength [B(GT)] distribution over different energy regions in the level scheme of the daughter nucleus. These single numbers do not provide information about the detailed structure of the B(GT) distribution that is used to calculate $T_{1/2}$ and P_n. Furthermore, the summation in the calculation in-

* adombos@nd.edu; Present address: Department of Physics and Joint Institute for Nuclear Astrophysics, University of Notre Dame, Notre Dame, Indiana 46556, USA
† Present address: Pacific Northwest National Laboratory, Richland, WA 99352, USA
‡ Present address: P. Moller Scientific Computing and Graphics, P. O. Box 75009 Honolulu, HI 96836-0009

troduces the possibility of obtaining the same $T_{1/2}$ and P_n values from different B(GT) distributions (for example, see Fig. 10 of Ref. [5] and Figs. 10–11,14–15 of Ref. [6]). This possibility casts uncertainty on which theoretical models are most reliable for applications to nuclides relevant to the r process, where experimental data are nonexistent and experiments are currently unfeasible. A superior approach would be to compare the theoretical models to the experimental B(GT) distribution, because this distribution is sensitive to the nuclear structure [7–9].

The A = 100–110 mass region is an intermediate mass region that can be studied at current experimental facilities, and nuclides in this region are expected to have an appreciable amount of low-lying B(GT) [10] that can be extracted with β decay. Experimental B(GT) distributions in this mass region can be used to constrain theoretical models and provide more confidence in the reliability of these models far from stability. The A = 100–110 mass region is also characterized by rapid changes in nuclear structure [11]. For nuclides in this mass region, a comparison of theoretical and experimental B(GT) distributions may be used to learn about the shape (spherical, oblate, or prolate) of the ground state of the parent nucleus. This idea was proposed by I. Hamamoto et al. for neutron-deficient nuclides in the $28 < Z < 66$ region [12, 13], explored further by P. Sarriguren et al. for neutron-deficient and neutron-rich nuclides [5, 6, 14–25], and experimentally studied by the Valencia-Strasbourg-Madrid-Surrey and Valencia-Nantes-Surrey-Jyväskylä collaborations [26–33]. Similar studies of deformation effects on B(GT) were performed in the rubidium isotope chain [7]. Nuclides in the A = 100–110 mass region have been shown to have different B(GT) distributions depending on the ground-state shape of the parent nucleus [5, 6].

In the present work, the B(GT) distributions of nuclides in the A = 100–110 mass region were extracted. Specifically, the β-decay feeding intensity distributions of ^{101,102}Zr and ^{109}Tc were obtained experimentally, and converted to B(GT) distributions. The β-decay feeding intensity distributions were extracted using the total absorption spectroscopy (TAS) technique [9] to avoid systematic errors from the Pandemonium effect [34]. The β-decay feeding intensity and B(GT) distributions were compared to three different quasiparticle random-phase approximation (QRPA) models based on different mean-field potentials. These comparisons were performed to learn about the ground-state shape of the parent nucleus and test models commonly used to provide β-decay properties in r-process network calculations.

In addition to nuclear astrophysics and nuclear structure, TAS measurements in this mass region have implications in other areas of fundamental and applied science. For example, other technetium isotopes near ^{109}Tc have been studied with the TAS technique. The β decay of ^{100}Tc was studied to provide experimental data in the A = 100 isobaric chain in order to constrain theoretical models used in double β decay calculations of ^{100}Mo [35]. The β decays of ^{102,104,105,106,107}Tc were studied in order to assess their impact on the production of decay heat [28, 36] and antineutrino energy spectra [37] from nuclear reactors. Another example is that the International Atomic Energy Agency has deemed a TAS study of ^{101}Zr as "priority I" with regards to determining antineutrino energy spectra from nuclear reactors (see Tables 2 and 3 of Ref. [38]). Accurate antineutrino energy spectra are important for understanding fundamental properties of antineutrinos [39], and noninvasive monitoring of nuclear reactors [40–42].

The present paper is organized as follows. The experimental details are discussed in Sec. II, the TAS analysis is described in Sec. III, and the results of the TAS analysis are presented in Sec. IV. The experimental results are compared to QRPA calculations relevant to nuclear structure in Sec. V and nuclear astrophysics in Sec. VI. A summary of the paper is presented in Sec. VII.

II. EXPERIMENTAL DETAILS

The experiment was the first-ever application of the TAS technique with a fast beam produced via projectile fragmentation, and was performed at the National Superconducting Cyclotron Laboratory (NSCL) at Michigan State University. The experimental details were described in Ref. [43], and are briefly described here.

The Coupled Cyclotron Facility produced a primary beam of ^{124}Sn^{45+} with an energy of 120 MeV/u, which impinged upon a ^{9}Be production target with a thickness of 403 mg/cm^2. The resulting ions were filtered with the A1900 fragment separator [44] to produce a secondary cocktail beam that consisted of neutron-rich nuclides with atomic numbers ranging from 39 to 43 and mass numbers ranging from 100 to 110. After the A1900 fragment separator, the ions were delivered to the experimental end station, which consisted of two silicon PIN detectors, an implantation station, and the Summing NaI(Tl) (SuN) detector. The implantation station consisted of a double-sided silicon-strip detector (DSSD) and a silicon surface barrier detector. Signals from all of the detectors in the end station were recorded with the NSCL Digital Data Acquisition System (DDAS) [45].

The implantation station was installed in the center of the borehole of SuN. The DSSD was positioned at the geometric center of SuN, and was used to detect high-energy ion implantations and subsequent low-energy β-decay electrons, which were spatially and temporally correlated to one another [46]. The silicon chip of the DSSD had a thickness of 1030 μm, dimensions of 21.8 mm by 21.8 mm, and an active area of 20.0 mm by 20.0 mm. There were 16 horizontal strips on the front side and 16 vertical strips on the back side, effectively creating 256 pixels. All strips had a pitch of 1250 μm. Roughly 25 mm downstream from the DSSD was a silicon surface barrier detector (active area of 300 mm^2 and depletion depth

of 500 μm) that acted as a veto detector to detect any ions (particularly light, charged particles) that did not stop in the DSSD. Surrounding the implantation station was the SuN detector [47] to employ the TAS technique. SuN is a segmented total absorption spectrometer, with eight segments of NaI(Tl). The individual segments of SuN provide a way of performing low-resolution, discrete γ-ray spectroscopy, while the entire detector is used as a calorimeter to apply the TAS technique.

The segmentation of SuN allows for the creation of many spectra that can be used in the TAS analysis to extract the β-decay feeding intensity distribution. One spectrum is the TAS spectrum, which is created by summing the energy deposition in all eight segments and is sensitive to the levels populated in the daughter nucleus. Another spectrum is the sum-of-segments spectrum, which is created by summing the histograms from each segment and is sensitive to the individual γ-ray transitions between levels. Another spectrum is the multiplicity spectrum, which is created by recording the number of segments that participated in the event and is sensitive to the number of γ rays from the deexcitation of the populated levels. Other spectra can be created with different gating conditions and also used in the TAS analysis.

III. ANALYSIS

With a segmented total absorption spectrometer, a spectrum can be labeled with the subscript i (for example, one value of i could correspond to the TAS spectrum, and another value of i could correspond to the sum-of-segments spectrum). In spectrum i, a bin can be labeled with the subscript j. The number of counts in bin j is affected by the population of different levels in the daughter from β decay. A level can be labeled with the subscript k. Therefore, using a modified version of the notation developed in Ref. [48], the experimental spectra obtained with a segmented total absorption spectrometer are described as

$$d_{ij} = \sum_k R_{ijk} f_k + \sum_l C_{ijl}, \tag{1}$$

where d_{ij} is the number of counts in bin j of experimental spectrum i, R_{ijk} is the detector response function with counts in bin j of spectrum i due to the population of level k in the daughter from β decay, f_k is the number of β decays that feed level k, and C_{ijl} is the number of counts in bin j of spectrum i due to contamination from source l.

The detector response functions of SuN, R_{ijk} in Eq. 1, were modeled with GEANT4 [49] and included phenomena associated with the β-decay transition from the initial level of the parent to the final level of the daughter nucleus, and the possible subsequent electromagnetic deexcitation of the final level. These phenomena included the β-decay electron with a realistic kinetic energy distribution [50], and any γ-ray cascades to the ground state or isomeric state(s) of the daughter. The simulated and experimental spectra had the same coincidence requirements and detector thresholds. As mentioned in Ref. [43], the thresholds for the strips in the high-gain stage of the DSSD ranged from 150 to 200 keV. Two distinct types of levels populated in the daughter were simulated: known levels at discrete energies and pseudo levels within a quasi-continuum. The boundary between these two types of levels was called the critical energy (sometimes referred to as the cutoff energy).

Known levels were below the critical energy, where the level scheme was assumed to be complete in terms of energies, spins, parities, and branching ratios. The Reference Input Parameter Library (RIPL-3) [51] contained a suggested value of the critical energy for the daughter nuclides ^{101,102}Nb and ^{109}Ru. In the present work, the critical energy was determined by comparing the experimental TAS and sum-of-segments spectra with those obtained from simulation using the existing decay scheme as found in an Evaluated Nuclear Structure Data File (ENSDF) [52]. With this method, the critical energy was different from the RIPL-3 suggested value (Table I). Information about known levels usually came from high-resolution measurements obtained with high-purity germanium detectors, although segmented total absorption spectrometers may also be used to estimate some of this information [53].

The energies, spins, and parities of known levels and the relative γ-ray intensities for transitions between known levels were taken from ENSDF [52]. Transitions included the possibility of internal conversion according to internal conversion coefficients calculated using BrIcc [54]. In the case of β decay directly populating either the ground state or β-decaying isomeric state(s) of the daughter, the detector response function was produced only from collisional energy losses between β-decay electrons and the sensitive volume of SuN or the associated bremsstrahlung radiation.

Some known levels had unknown or tentative spin and/or parity assignments. This information determined the probability of internal conversion and affected transitions from the quasi-continuum to known levels. In these cases, multiple level schemes were constructed that differed in the spin and/or parity assignments and used in the TAS analysis to assess uncertainties in the extracted β-decay feeding intensity distribution.

Above the critical energy, a quasi-continuum was assumed to exist, which was divided into energy bins. At the center of each energy bin was placed a pseudo level, which acted as a representative for all nearby levels within the energy resolution of SuN. The spacing between pseudo levels was dependent on the energy resolution of SuN: Because the full width at half maximum increases as the energy increases, the spacing between pseudo levels (equivalently, the size of each energy bin) increased as the energy increased. For example, the spacing between pseudo levels near 2000 keV was approximately 100 keV, whereas the spacing between pseudo levels near 3000 keV

was approximately 150 keV.

The γ-ray cascades from pseudo levels were created with the statistical model as implemented in DICEBOX [55]. In DICEBOX, the user inputs as much information as possible about the known levels (for example, energies, spins, parities, relative γ-ray intensities, and total internal conversion coefficients). The user also gives as input the critical energy (E_{crit}). Above the critical energy, the program uses statistical properties to describe how levels are distributed and how they deexcite with γ rays. These statistical properties are the nuclear level density (NLD) and γ-ray strength functions (γSFs) for E1, M1, and E2 transitions. When running DICEBOX to generate γ-ray cascades from a pseudo level, the user gives as input the energy, spin, and parity of the pseudo level. Between the energy of the pseudo level and the critical energy, DICEBOX generates a set of levels using the nuclear level density. Transitions between levels in the quasi-continuum and transitions between a level in the quasi-continuum to a known level are governed by the γ-ray strength function. When a transition reaches a known level, the transitions between known levels are determined by the input relative γ-ray intensities and total internal conversion coefficients. This procedure is repeated for all pseudo levels within the quasi-continuum. Other implementations of the statistical model to create γ-ray cascades can be found in DECAYGEN [56], DEGEN [57], CASCADE [58–61], γDEX [62], and RAINIER [63].

The relevant features of DICEBOX in the creation of the γ-ray cascades were the choice of a NLD, γSFs for E1, M1, and E2 transitions, and E_{crit}. The NLD came from the Hartree-Fock-Bogoliubov plus combinatorial method [64], the E1 γSF was modeled as a modified Lorentzian with a constant nuclear temperature (0.5 MeV), and the M1 γSF and E2 γSF were modeled as standard Lorentzians. The resonance energy, width, and peak cross section for the E1 γSF were taken from experimental measurements compiled in RIPL-3, and for the M1 γSF and E2 γSF were taken from systematics according to RIPL-3 [51]. Table I contains the relevant parameters used in DICEBOX for the different nuclides in the present work.

The spins and parities of pseudo levels were determined using β-decay selection rules assuming allowed Gamow-Teller transitions ($\Delta J = 0, \pm 1$; $\Delta\pi = +$; no 0^+ to 0^+). For a given energy of a pseudo level, the different spins will decay differently via E1, M1, and E2 transitions within the quasi-continuum and from the quasi-continuum to a known level. Including the different spins was important because the summing efficiency of SuN depends on how the deexcitation of a pseudo level is partitioned in terms of number of γ rays and their individual energies [47]. To reduce the number of detector response functions used in the TAS analysis, an average detector response function was created from the different spins.

The potential sources of contamination, C_{ijl} in Eq. 1, included room background, electronic pulse pileup, random correlations of implantation and decay events, charge-state contamination, and β-decay progeny. Each potential source was investigated and included in the TAS analysis if necessary.

The experimental spectra used in the TAS analysis were obtained by correlating decay events to implantation events with spatial and temporal information. Decay events were naturally gated by a β-decay electron, producing β-gated spectra. A 2 μs coincidence time window was used to create events, which reduced the probability of recording room background during a decay event. Therefore, contamination from room background was negligible.

Electronic pulse pileup will depend on the counting rate of each of SuN's PMTs during the experiment. Throughout the experiment, the average counting rate was approximately 900 Hz. For only decay events from all nuclides implanted into the DSSD, the average counting rate was approximately 7 Hz for PMTs of the central segments, and approximately 1 Hz for PMTs of the outer segments. This low counting rate meant contamination from electronic pulse pileup was negligible.

The secondary beam was defocused to try to illuminate as much of the surface of the DSSD as possible, and the implantation rate was approximately 10 implantations per second. For central pixels, there was on average approximately 0.25 observed decays per second. Within the correlation procedure, not all decay events were correlated to the correct implantation event, resulting in random correlations. These random correlations arose from many different scenarios that occurred throughout the experiment. One scenario involved the accumulated activity in the DSSD. For each implanted ion in the experiment, an average of 4–5 β decays were necessary to reach stability. This accumulated activity in the DSSD from the relatively long decay chains created a persistent background of decay events. Decays from this persistent background may have been incorrectly correlated to an implantation. Because the half-lives of the implanted ions are on the order of seconds, the correlation time window was relatively large in order to correctly correlate a decay to an implantation and collect enough statistics in the experimental β-delayed γ-ray spectra for the TAS analysis. However, a relatively large correlation time window came at the expense of an increase in random correlations due to the persistent background of decays events. Another scenario that contributed to random correlations occurred when a later implantation was localized in the same spatial region of the DSSD as an earlier implantation, but before the earlier implantation underwent β decay. If the earlier implantation then underwent β decay, then the decay of the earlier implantation was incorrectly correlated to the later implantation (in the present work, decay events were only correlated to the most recent implantation in the correlation field). A third scenario that contributed to random correlations occurred when an earlier implantation was localized to one pixel and the subsequent β-decay electron was localized to a different pixel. This was because the β-decay

TABLE I. The values used for different parameters in DICEBOX when creating pseudo levels above E_{crit} (critical energy) for the three daughter nuclides in the present work. The parameters associated with giant resonances that were needed for the γ-ray strength functions were E_r (resonance energy), Γ (width), and σ (peak cross section). The parameters for the E1 γ-ray strength function were from the nearest nuclide of the same type (even Z and even N, even Z and odd N, etc.) for which experimental measurements exist in RIPL-3. However, there were no odd Z and odd N measurements near $^{102}_{41}Nb_{61}$ and therefore the nearest measurement was used regardless of even/odd proton/neutron numbers. The nearest nuclides for $^{101}_{41}Nb_{60}$, $^{102}_{41}Nb_{61}$, and $^{109}_{44}Ru_{65}$ were $^{103}_{45}Rh_{58}$, $^{100}_{42}Mo_{58}$, and $^{117}_{50}Sn_{67}$, respectively. The final results of this work were not sensitive to small variations in these parameters.

		γ-ray strength function parameters								
		E1			M1			E2		
Nuclide	E_{crit} [keV]	E_r [MeV]	Γ [MeV]	σ [mb]	E_r [MeV]	Γ [MeV]	σ [mb]	E_r [MeV]	Γ [MeV]	σ [mb]
$^{101}_{41}Nb_{60}$	2119	16.62	8.56	187.50	8.80	4.00	1.76	13.53	4.90	2.02
$^{102}_{41}Nb_{61}$	941	16.02	8.44	167.00	8.78	4.00	1.72	13.48	4.89	2.01
$^{109}_{44}Ru_{65}$	1268	15.64	5.02	257.50	8.58	4.00	1.49	13.19	4.80	2.20

electron had a maximum energy deposition in that pixel. In between those two events, a later implantation was localized in the same pixel as the one where the β-decay electron from the earlier implantation will be localized. The decay of the earlier implantation was then incorrectly correlated to the later implantation. These random correlations were characterized by performing correlations backward in time [65].

The relatively heavy nuclides in the present work meant that not all ions were fully stripped of electrons, resulting in charge-state contamination in the particle identification spectrum. For example, hydrogen-like $^{98}_{40}Zr^{39+}$ had a similar mass-to-charge ratio as fully stripped $^{101}_{40}Zr^{40+}$. This made $^{98}_{40}Zr^{39+}$ a charge-state contaminant of the ion of interest $^{101}_{40}Zr^{40+}$. Charge-state separation is usually accomplished by measuring the total kinetic energy of ions, but this was not possible in the present work because implantation events saturated the DSSD preamplifiers. Alternative methods to reduce charge-state contamination will be described individually for each nuclide.

Depending on the half-life of the daughter for a given nuclide, there may be contamination from the decay of the daughter within the correlation time window. Methods to estimate or eliminate contamination from the decay of the daughter will be described individually for each nuclide.

Once the contamination was accounted for as best as possible, the detector response functions were used to simultaneously fit all the experimental spectra by minimizing the global χ^2 value

$$\chi^2_{\text{global}} = \sum_i \sum_j \left(\frac{d_{ij} - \sum_k R_{ijk} f_k - \sum_l C_{ijl}}{\sqrt{d_{ij}}} \right)^2 . \quad (2)$$

The experimental spectra included in the calculation of χ^2_{global} included a total of nine spectra with various gates or restrictions applied to them. The nine spectra were the TAS spectrum, sum-of-segments spectrum, multiplicity spectrum, and the sum-of-segments and multiplicity spectra gated on the TAS spectrum from 0–800 keV, 800–2500 keV, and 2500 keV to the end of the TAS spectrum. These three energy regions were appropriate based on the statistics in the gated spectra. All nine spectra were included in the calculation to further constrain the summing efficiency of SuN, make the TAS analysis more sensitive to the finer details of the decay scheme, and help find the true minimum in the χ^2_{global} space. In addition, after minimizing χ^2_{global}, the initial number of decaying nuclei was compared between experiment and simulation. This comparison was performed to assess uncertainties in the extracted β-decay feeding intensity distribution.

Three different sources of uncertainty contributed to the total uncertainty in the β-decay feeding intensity distribution. The first source of uncertainty was from the statistics of the TAS spectrum. The inherent statistical uncertainty in the number of counts per bin in the TAS spectrum is directly related to the uncertainty in the extracted β-decay feeding intensity distribution. The second source of uncertainty was from spin/parity variations in the level schemes of the daughter (Sec. III). For each excitation energy, the minimum, average, and maximum intensity using the different level schemes was calculated. The difference between the average and the minimum (maximum) intensity contributed to the lower (upper) bound on the uncertainty. The third source of uncertainty was from the ground-state-to-ground-state transition or transition from the ground state to the β-decaying isomeric state, depending on the nuclide.

In Eq. 2, the number of decays feeding each level was repeatedly adjusted until χ^2_{global} was minimized. The number of decays feeding each level was then normalized to unity to obtain the β-decay feeding intensity distribution

$$I_{\beta_i} = \frac{f_i}{\sum_k f_k}. \quad (3)$$

The first demonstration of SuN's ability to extract β-decay feeding intensity distributions with the TAS technique was presented in Ref. [66]. The β-decay feeding

intensity distribution was then converted to a B(GT) distribution

$$B(\mathrm{GT}, E_{\mathrm{ex}}) = K \left(\frac{g_V}{g_A}\right)^2 \frac{I_\beta(E_{\mathrm{ex}})}{f(Q_\beta - E_{\mathrm{ex}})T_{1/2}}, \quad (4)$$

where E_{ex} is the excitation energy, $K = 6143.6(17)$ s [67], $g_A/g_V = -1.270(3)$ [68], I_β is the β-decay feeding intensity to a particular excitation energy, $f(Q_\beta - E_{\mathrm{ex}})$ is the dimensionless Fermi integral corresponding to a particular excitation energy, Q_β is the ground-state-to-ground-state Q value for β decay, and $T_{1/2}$ is the β-decay half-life. The units of B(GT) using Eq. 4 are $g_A^2/4\pi$.

IV. RESULTS

A. $^{101}_{40}\mathbf{Zr}_{61} \rightarrow {}^{101}_{41}\mathbf{Nb}_{60}$

The half-life of the parent ^{101}Zr is 2.27(12) s [43], the daughter ^{101}Nb is 7.1(3) s [69], and the charge-state contaminant ^{98}Zr^{39+} is 30.7(4) s [70]. Because the experimental spectra used in the TAS analysis were obtained with a correlation time window of one second, the amount of contamination from the decay of the charge-state contaminant was negligible (less than 5%). Contamination from the daughter was estimated with spectra obtained with a later correlation time window (6 to 7 s). These spectra were scaled by the Bateman equations [71] to estimate their contribution in the correlation time window used in the TAS analysis (0 to 1 s). The ground-state-to-ground-state Q value for the β decay of the parent ^{101}Zr is 5726 keV, while the one-neutron separation energy of the daughter ^{101}Nb is 7165 keV [72], making β-delayed neutron emission energetically impossible.

Detector response functions were created for known levels populated in β decay below the critical energy. They were created using information from the existing level scheme of the daughter from ENSDF [69]. All levels below the critical energy have unknown or tentative spin and parity assignments, and therefore four level schemes were constructed with different spin and parity assumptions. The different level schemes contributed to the uncertainty in the extracted β-decay feeding intensity distribution. There were a total of 36 detector response functions for known levels, starting at 0 keV and ending at 2119 keV.

Detector response functions were created for pseudo levels above the critical energy. The spin and parity of the ground state of the parent ^{101}Zr is $(3/2^+)$ [69]. According to β-decay selection rules for allowed Gamow-Teller transitions, the states populated in the daughter are $1/2^+$, $3/2^+$, and $5/2^+$. Following these rules, γ-ray cascades from three pseudo levels were created with DICEBOX for each energy bin in the quasi-continuum. These three pseudo levels had corresponding detector response functions created with GEANT4, from which an average detector response function was created and used in the TAS analysis. There were a total of 17 average detector response functions for pseudo levels, starting at 2220 keV (where the total level density is approximately 0.23 / keV [64] and the energy resolution of SuN is approximately 115 keV) and ending at 4195 keV (where the total level density is approximately 5.57 / keV [64] and the energy resolution of SuN is approximately 173 keV).

The TAS spectrum, sum-of-segments spectrum, and multiplicity spectrum are shown in Fig. 1. One dominating feature of the TAS spectrum is the sum peak from a group of levels (specifically, those levels between 1878.1 keV and 2030.65 keV, inclusive) that collectively have a relatively large β-decay feeding intensity. Previous fission-based experiments [73, 74] also observed that collectively these levels were strongly fed in β decay. In the present work, the total β-decay feeding intensity assigned to these levels is between 22.2% and 25.0%. This agrees with the decay scheme of Ref. [74] which has minimum and maximum values of 14.1% and 24.9%, respectively.

Another dominating feature of the TAS spectrum is the ground-state-to-ground-state transition. The ground-state-to-ground-state transition does not emit any characteristic γ rays, and instead appears as a broad continuum from the interaction of the emitted electrons with SuN. The ground-state-to-ground-state transition was included as one of the response functions in the fitting procedure. In the decay scheme of Ref. [74], the β-decay feeding intensity assigned to the ground-state-to-ground-state transition is 57(11)%. In the present work, the β-decay feeding intensity for the ground-state-to-ground-state transition is $51.2^{+2.8}_{-12.2}$%, in agreement with the previous measurement [74].

In the sum-of-segments spectrum, noticeable features include peaks corresponding to γ rays with a relatively large absolute γ-ray intensity [69]. This includes a peak corresponding to the 119.3 keV γ ray, a peak corresponding to the 205.7 keV and 208.5 keV γ rays, and a broad peak corresponding to γ rays with energies between 1810.1 keV and 2009.5 keV.

The β-decay feeding intensity distribution of ^{101}Zr as a function of excitation energy in the daughter nucleus ^{101}Nb is reported in Table II. The β-decay feeding intensity distribution in Table II is an average of the different level schemes assumed for the daughter (Sec. III). The amount of β-decay feeding intensity to known levels is 91.4% and to pseudo levels is 8.6%. The weighted average of the uncertainty was 10% from statistics, and 2% from multiple level schemes. The uncertainty from the ground-state-to-ground-state transition is discussed below.

Extracting the β-decay feeding intensity for the ground-state-to-ground-state transition relies on the collisional energy losses between β-decay electrons and the sensitive volume of SuN or the associated bremsstrahlung radiation. Because the β-decay electrons lose energy in materials encountered prior to reaching the NaI(Tl) in SuN and their energy spectrum is broad, and no characteristic γ rays are emitted, identifying the signature of

TABLE II. The β-decay feeding intensity distribution of ^{101}Zr as a function of excitation energy in the daughter nucleus ^{101}Nb. Intensity values below 10^{-4}% are set to 0.

Energy (keV)	Intensity (%)	Error (–)	Error (+)	Energy (keV)	Intensity (%)	Error (–)	Error (+)
0	51.2	12.2	2.8	1844	0.0002	0.0002	0.0003
119	0.0002	0.0002	0.0003	1878	8.01	0.43	0.43
206	0.0001	0.0001	0.0001	1925	3.92	0.26	0.26
208	0	0	0	1929	0.0038	0.0038	0.0032
255	0.0000	0.0000	0.0001	1958	4.15	0.23	0.25
346	0.0011	0.0011	0.0024	2010	1.98	0.11	0.14
374	1.94	0.25	0.26	2031	5.51	0.31	0.31
532	0.0000	0.0000	0.0001	2096	0.010	0.010	0.015
593	2.95	0.50	0.51	2119	1.78	0.13	0.13
598	0.0000	0.0000	0.0001	2220	0.837	0.092	0.094
673	1.21	0.18	0.18	2320	0.016	0.015	0.035
703	0.0014	0.0014	0.0017	2420	1.20	0.18	0.18
722	0.68	0.15	0.15	2520	0.0013	0.0013	0.0021
778	0	0	0	2620	0.350	0.171	0.098
782	0.90	0.14	0.14	2720	0.0001	0.0001	0.0001
879	0.025	0.024	0.016	2820	0.34	0.12	0.24
900	0	0	0	2920	1.40	0.25	0.19
912	2.08	0.28	0.28	3020	0.012	0.012	0.015
922	0.013	0.009	0.015	3145	0.84	0.15	0.15
953	0	0	0	3295	0.0001	0.0001	0.0002
1061	0.0020	0.0020	0.0025	3445	1.27	0.27	0.28
1110	0	0	0	3595	1.28	0.27	0.27
1120	0.0015	0.0015	0.0029	3745	0.47	0.20	0.19
1126	0	0	0	3895	0.0001	0.0001	0.0001
1180	3.12	0.32	0.32	4045	0.53	0.16	0.16
1294	0.0012	0.0011	0.0020	4195	0.109	0.065	0.065
1620	1.89	0.20	0.20				

this transition is difficult and the sensitivity of SuN to this type of transition is reduced. An additional analysis procedure was performed to test the sensitivity of SuN to the ground-state-to-ground-state transition.

The β-decay feeding intensity was fixed for the ground-state-to-ground-state transition while the β-decay feeding intensity was allowed to vary for all other levels. In total, 100 fits were performed. In these fits, the β-decay feeding intensity was fixed for the ground-state-to-ground-state transition between 0–1%, 1–2%, ..., 98–99%, 99–100%. For each fit, the reduced χ^2_{global} was calculated. The ground-state-to-ground-state transition probability in the β-decay feeding intensity distribution reported in Table II was also the minimum of the reduced χ^2_{global} distribution of the 100 fits. Additionally, for each of the 100 fits, the initial number of decaying nuclei with uncertainty of ^{101}Zr was calculated using the β-decay feeding intensity distribution of each fit and the detection efficiency of SuN. The initial number of decaying nuclei with uncertainty from each fit was then compared to the experimental value with uncertainty (in this case, the number of decay events correlated to ^{101}Zr implantations). The calculated initial number of decaying nuclei for the fit that had the ground-state-to-ground-state transition probability reported in Table II was in agreement with the experimental value, within the uncertainty. The uncertainty in the agreement contributed to the uncertainty in the reported ground-state-to-ground-state transition probability.

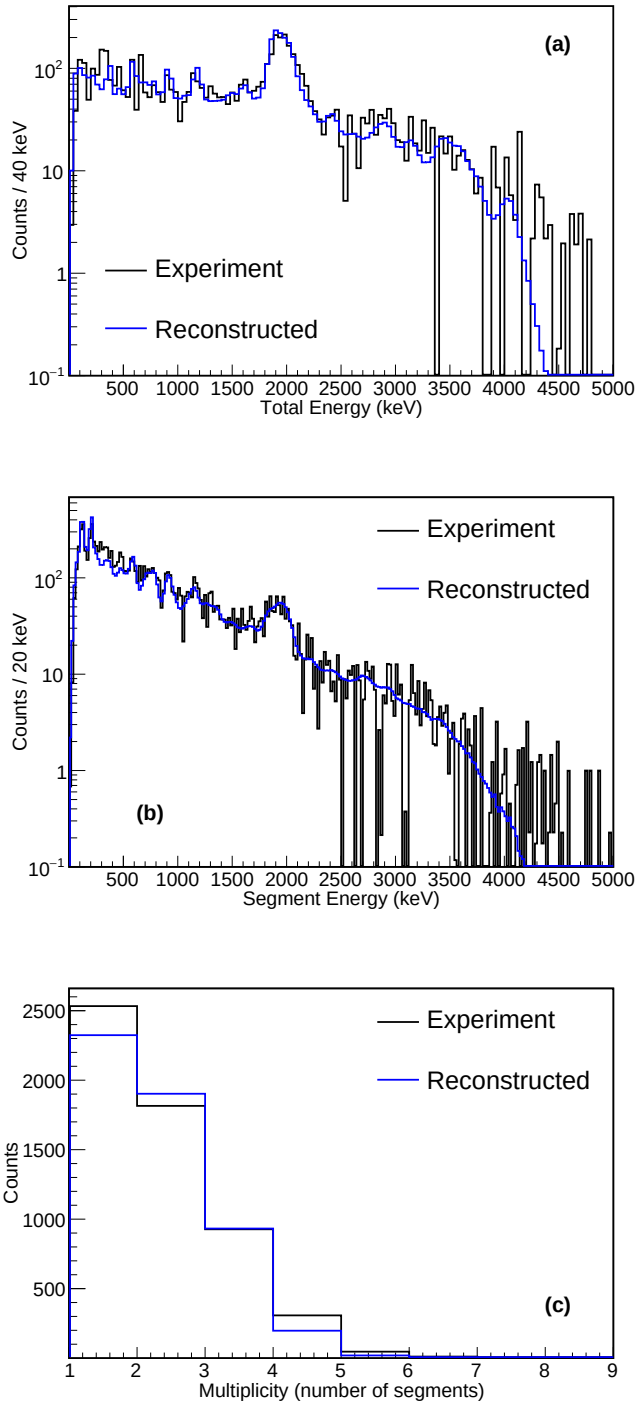

FIG. 1. (Color online) Comparison of experimental (black, solid line) and reconstructed (blue, solid line) spectra from the β decay of ^{101}Zr for the (a) TAS spectrum, (b) sum-of-segments spectrum, and (c) multiplicity spectrum. The experimental spectra were obtained by correlating decay events to ^{101}Zr implantations with a correlation time window of one second. Contamination from random correlations and the decay of the daughter has been subtracted from the experimental spectra. The ground-state-to-ground-state Q value for the β decay of ^{101}Zr is 5726 keV [72].

B. $^{102}_{40}\mathrm{Zr}_{62} \rightarrow {}^{102}_{41}\mathrm{Nb}_{61}$

The half-life of the parent ^{102}Zr is 2.01(8) s [43], the daughter ^{102m}Nb is 1.33(27) s [43], and the charge-state contaminant ^{99}Zr^{39+} is 2.1(1) s [75]. Contamination from the daughter was estimated with spectra obtained with a later correlation time window (6 to 7 s). These spectra were scaled by the Bateman equations [71] to estimate their contribution in the correlation time window used in the TAS analysis (0 to 1 s). Charge-state contamination from ^{99}Zr^{39+} was additionally minimized with conservative gates in the particle identification spectrum. No features associated with the charge-state contamination were observed in the final spectra, and the amount of contamination was estimated to be less than 5%. The ground-state-to-ground-state Q value for the β decay of the parent ^{102}Zr is 4717 keV, while the one-neutron separation energy of the daughter ^{102}Nb is 5484 keV [72], making β-delayed neutron emission energetically impossible.

The half-life extracted from a decay curve gated simultaneously on the TAS and sum-of-segments spectra led to the conclusion that the β decay of ^{102}Zr populates levels in ^{102}Nb that are built on top of the β-decaying isomeric state [43]. The same conclusion was found in Ref. [76], and therefore the excitation energy, x = 93 keV, of the β-decaying isomeric state was included in the energy of the states here.

Similar to the process described for ^{101}Zr, detector response functions were created for known levels from ENSDF [77] populated in β decay below the critical energy. There were a total of 12 detector response functions for known levels, starting at 0+x keV and ending at 941+x keV.

The level at 20+x keV has a single transition to the level at 0+x keV. This transition has a large total internal conversion coefficient [76, 77]. Any radiation emitted during this transition, regardless of whether or not internal conversion occurred, is below the detection threshold of SuN. As a consequence, the detector response functions for the levels at 0+x keV and 20+x keV were nearly identical, and a single detector response function was used for both levels in the TAS analysis at 0+x keV.

Detector response functions were also created for pseudo levels above the critical energy. The spin and parity of the ground state of the parent ^{102}Zr is 0^+ [77]. According to β-decay selection rules for allowed Gamow-Teller transitions, the states populated in the daughter are 1^+. Following these rules, γ-ray cascades from one pseudo level was created with DICEBOX for each energy bin in the quasi-continuum. Each pseudo level had a corresponding detector response function created with GEANT4. There were a total of 28 detector response functions for pseudo levels, starting at 1000+x keV (where the total level density is approximately 0.08 / keV [64] and the energy resolution of SuN is approximately 71 keV) and ending at 3000+x keV (where the total level density is approximately 3.50 / keV [64] and the energy

resolution of SuN is approximately 143 keV).

The TAS spectrum, sum-of-segments spectrum, and multiplicity spectrum are shown in Fig. 2. The sum peak corresponding to the level at 599.48+x keV is one of the dominating features in the TAS spectrum. A previous experiment studying the β decay of ^{102}Zr assigned a β-decay feeding intensity of 25(2)% to this level [76, 77]. In the present work, the β-decay feeding intensity extracted for this level is $23.1^{+1.5}_{-1.5}$%, in agreement with the previous measurement [76, 77].

The transition from the ground state to the β-decaying isomeric state is another dominating feature of the TAS spectrum. In the decay scheme of Ref. [76, 77], an upper limit of 59(3)% was assigned to the transition from the ground state to the β-decaying isomeric state. In the present work, the β-decay feeding intensity for the transition from the ground state to the β-decaying isomeric state is 45.0^{+7}_{-9}%. This value is consistent with the upper limit placed by the authors of the decay scheme in Ref. [76]. An upper limit could only be placed on the transition from the ground state to the β-decaying isomeric state in Ref. [76] because the decay scheme ended at 940.5+x keV. With a ground-state-to-ground-state Q value for the β decay of ^{102}Zr at 4717 keV [72], the authors of Ref. [76] noted that there was probably some β-decay feeding intensity to higher-lying levels that was missed due to their limited detection sensitivity.

Peaks corresponding to γ rays with a relatively large absolute γ-ray intensity [69] can be seen in the sum-of-segments spectrum. There are peaks corresponding to γ-ray energies of 64.46, 152.4, 156.14, 535.13, and 599.48 keV. The strongest transitions observed in Ref. [76] had energies of 64 keV, 535 keV, and 599 keV.

The β-decay feeding intensity distribution of ^{102}Zr as a function of excitation energy in the daughter nucleus ^{102}Nb is reported in Table III. The β-decay feeding intensity distribution in Table III is the result of the single level scheme assumed for the daughter. The amount of β-decay feeding intensity to known levels is 74.6% and to pseudo levels is 25.4%. The weighted average of the uncertainty from statistics was 13%. There was only one level scheme assumed for ^{102}Nb, so there was no uncertainty from multiple level schemes. The uncertainty from the transition from the ground state to the β-decaying isomeric state is discussed below.

The analysis procedure for determining the uncertainty in the transition from the ground state to the β-decaying isomeric state was already discussed for the similar case (ground-state-to-ground-state transition) of ^{101}Zr in Sec. IV A. From this procedure, an additional β-decay feeding intensity distribution that fit the experimental spectra was obtained, in which the transition probability from the ground state to the β-decaying isomeric state was held fixed between 60% and 61% (Table IV). Extracting the transition from the ground state to the β-decaying isomeric state in TAS measurements is a challenging task. Since we cannot exclude any of the two sets of β-decay feeding intensity distributions

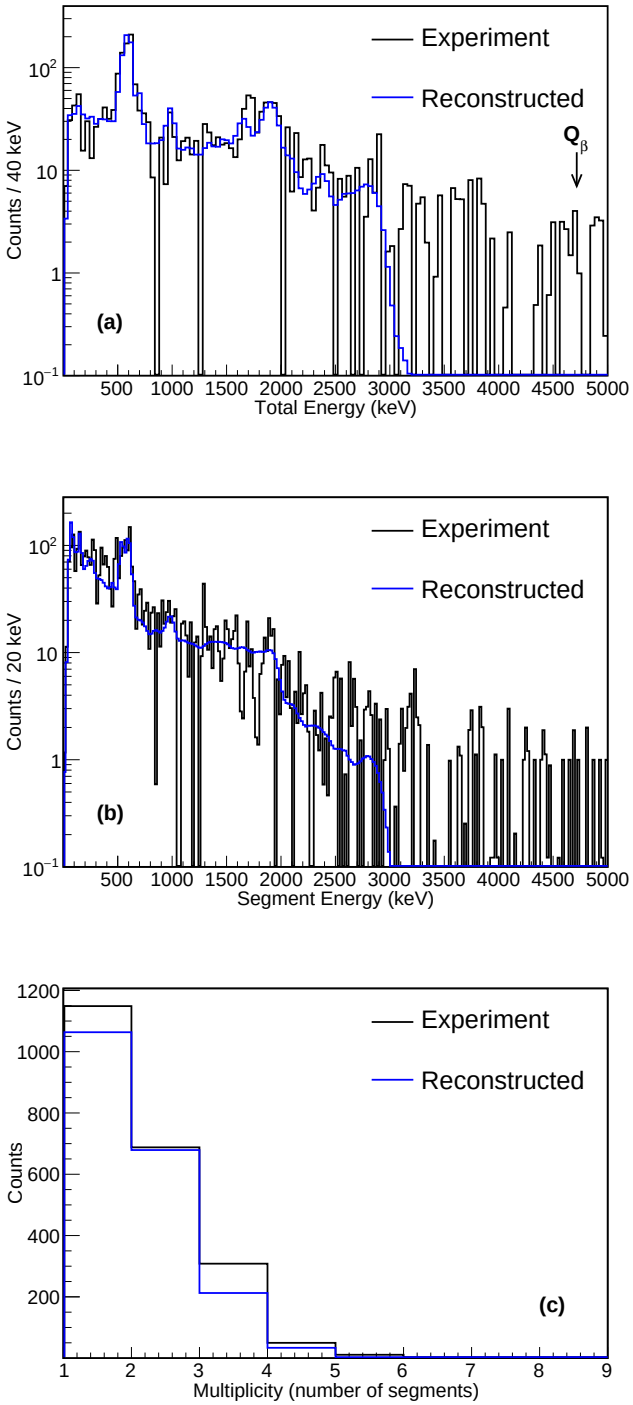

FIG. 2. (Color online) Comparison of experimental (black, solid line) and reconstructed (blue, solid line) spectra from the β decay of ^{102}Zr for the (a) TAS spectrum, (b) sum-of-segments spectrum, and (c) multiplicity spectrum. The experimental spectra were obtained by correlating decay events to ^{102}Zr implantations with a correlation time window of one second. Contamination from random correlations and the decay of the daughter has been subtracted from the experimental spectra. There is a label for the ground-state-to-ground-state Q value in the TAS spectrum for the β decay of ^{102}Zr at 4717 keV [72].

TABLE III. The β-decay feeding intensity distribution of ^{102}Zr as a function of excitation energy in the daughter nucleus ^{102}Nb. Intensity values below 10^{-4}% are set to 0. As explained in Sec. IV B, each level was assumed to be built on top of the β-decaying isomeric state. That is, a value of x = 93 keV as determined by Ref. [76] should be added to each level. As explained in Sec. IV B, the detector response function for the level at 20+x keV was not used in the TAS analysis.

Energy (keV)	Intensity (%)	Error (–)	Error (+)	Energy (keV)	Intensity (%)	Error (–)	Error (+)
0	45.0	9.0	7.0	1480	1.18	0.28	0.28
20	0	0	0	1540	0	0	0
64	0.0003	0.0001	0.0001	1600	0	0	0
94	0	0	0	1660	2.82	0.39	0.39
156	0.74	0.13	0.13	1720	1.29	0.13	0.13
161	0	0	0	1780	0.0011	0.0001	0.0001
246	0	0	0	1840	0.828	0.094	0.094
258	0	0	0	1900	4.04	0.51	0.51
431	0.93	0.18	0.18	1960	4.17	0.62	0.62
599	23.1	1.5	1.5	2020	0	0	0
705	4.82	0.61	0.61	2100	1.57	0.36	0.36
941	0	0	0	2200	0.0333	0.0080	0.0080
1000	3.27	0.72	0.72	2300	0.087	0.021	0.021
1060	0	0	0	2400	1.36	0.33	0.33
1120	0.212	0.054	0.054	2500	0	0	0
1180	0.51	0.13	0.13	2600	0.59	0.14	0.14
1240	0	0	0	2700	0.59	0.13	0.13
1300	0	0	0	2800	0.98	0.35	0.35
1360	1.02	0.30	0.30	2900	0.89	0.22	0.22
1420	0	0	0	3000	0.0005	0.0004	0.0004

reported here, we present both, similar to Ref. [28] for ^{105}Tc. When comparing the experimental results to QRPA calculations relevant to nuclear structure in Sec. V and nuclear astrophysics in Sec. VI, the β-decay feeding intensity distribution reported in Table III was used because the fit that resulted in that distribution had the smallest reduced $\chi^2_{\rm global}$.

Additionally, the β-decay feeding intensity distribution of ^{102}Zr was recently estimated [33, 78, 79] with the Decay Total Absorption γ-ray Spectrometer (DTAS) [80]. As mentioned in the publication, due to the limited sensitivity of their analysis for this specific case, the transition from the ground state to the β-decaying isomeric state was held fixed to the 59% value from Ref. [76]. The TAS spectrum from the analysis with DTAS and the present work are qualitatively similar, although the statistics are different. It should be noted that the cumulative β-decay feeding intensity distribution of ^{102}Zr from the analysis with DTAS and the present work (Table IV) are in agreement within the uncertainty.

C. $^{109}_{43}\mathbf{Tc}_{66} \rightarrow {}^{109}_{44}\mathbf{Ru}_{65}$

The half-life of the parent ^{109}Tc is 0.87(7) s [43], the daughter ^{109}Ru is 34.4(2) s [81], and the charge-state contaminant ^{106}Tc^{42+} is 35.6(6) s [82]. Because the experimental spectra used in the TAS analysis were obtained with a correlation time window of one second, the amount of contamination from the decay of the daughter and charge-state contaminant was negligible (less than 3%). The ground-state-to-ground-state Q value for the β decay of the parent ^{109}Tc is 6456 keV, while the one-neutron separation energy of the daughter ^{109}Ru is 5148 keV [72], making β-delayed neutron emission energetically possible. However, previous experiments obtained β-delayed neutron emission probabilities of 0.08(2)% [83] and $\leq$ 1% [84]. Additionally, there was no evidence in the TAS spectrum of a sum peak around 7 MeV, which would have resulted from thermal neutron capture on the ^{23}Na or ^{127}I of SuN. Therefore, β-delayed neutron emission was not incorporated into the analysis.

Similar to ^{101,102}Zr, detector response functions were created for known levels populated in β decay below the critical energy. Creating the response functions involved using information from ENSDF [81] and also a recent

TABLE IV. The β-decay feeding intensity distribution of ^{102}Zr as a function of excitation energy in the daughter nucleus ^{102}Nb. Intensity values below 10^{-4}% are set to 0. As explained in Sec. IV B, each level was assumed to be built on top of the β-decaying isomeric state. That is, a value of x = 93 keV as determined by Ref. [76] should be added to each level. As explained in Sec. IV B, the detector response function for the level at 20+x keV was not used in the TAS analysis. As explained in Sec. IV B, the values reported in this table are from the fit in which the transition from the ground state to the β-decaying isomeric state was held fixed between 60 and 61%.

Energy (keV)	Intensity (%)	Error (–)	Error (+)	Energy (keV)	Intensity (%)	Error (–)	Error (+)
0	60.0	9.0	7.0	1480	0.50	0.12	0.12
20	0	0	0	1540	0	0	0
64	0	0	0	1600	0	0	0
94	0	0	0	1660	2.52	0.35	0.35
156	0	0	0	1720	0.533	0.056	0.056
161	0	0	0	1780	0	0	0
246	0	0	0	1840	1.07	0.12	0.12
258	0	0	0	1900	2.93	0.37	0.37
431	0.170	0.033	0.033	1960	3.15	0.47	0.47
599	17.1	1.1	1.1	2020	0	0	0
705	4.11	0.52	0.52	2100	1.15	0.26	0.26
941	0	0	0	2200	0.070	0.017	0.017
1000	2.19	0.48	0.48	2300	0	0	0
1060	0	0	0	2400	1.06	0.25	0.25
1120	0.271	0.070	0.070	2500	0	0	0
1180	0.040	0.011	0.011	2600	0.364	0.088	0.088
1240	0	0	0	2700	0.60	0.13	0.13
1300	0	0	0	2800	0.66	0.23	0.23
1360	0.79	0.24	0.24	2900	0.72	0.18	0.18
1420	0	0	0	3000	0	0	0

high-resolution study of the β decay of ^{109}Tc [85].

All levels below the critical energy have tentative spin and parity assignments, and therefore four level schemes were constructed with different spin and parity assumptions. The different level schemes contributed to the uncertainty in the extracted β-decay feeding intensity distribution. There were a total of 21 detector response functions for known levels, starting at 0 keV and ending at 1268 keV.

Detector response functions were also created for pseudo levels above the critical energy, as described earlier. The spin and parity of the ground state of the parent ^{109}Tc is $(5/2^+)$ [81]. According to β-decay selection rules for allowed Gamow-Teller transitions, the states populated in the daughter are $3/2^+$, $5/2^+$, and $7/2^+$. Following these rules, γ-ray cascades from three pseudo levels were created with DICEBOX for each energy bin in the quasi-continuum. These three pseudo levels had corresponding detector response functions created with GEANT4, from which an average detector response function was created and used in the TAS analysis. There were a total of 33 average detector response functions for pseudo levels, starting at 1350 keV (where the total level density is approximately 0.07 / keV [64] and the energy resolution of SuN is approximately 82 keV) and ending at 5110 keV (where the total level density is approximately 25 / keV [64] and the energy resolution of SuN is approximately 194 keV).

The TAS spectrum, sum-of-segments spectrum, and multiplicity spectrum are shown in Fig. 3. There are many small sum peaks in the TAS spectrum. The transition in the daughter ^{109}Ru from the first excited state at 68.75 keV to the ground state has a total internal conversion coefficient of 4.97 [54, 81]. Many levels populated in β decay pass through the first excited state, which means that many γ-ray cascades will not emit a 68.75 keV γ ray but instead a conversion electron. This conversion electron will not deposit energy in SuN. There are other transitions in ^{109}Ru with non-negligible total internal conversion coefficients. As mentioned in Sec. III, internal conversion was included in the analysis. Due to internal conversion, counts for some of the sum peaks will be displaced by a certain energy, resulting in broadened sum peaks. Two larger sum peaks are noticeable at 1159.0 keV and 1267.8 keV.

The decay scheme of Ref. [81] assigned a β-decay feed-

ing intensity of 35(6)% for the ground-state-to-ground-state transition based on a measurement by Ref. [86]. Meanwhile, the decay scheme of Ref. [87] did not assign a β-decay feeding intensity for the ground-state-to-ground-state transition. In the current work, the β-decay feeding intensity for the ground-state-to-ground-state transition is $5.7^{+5.8}_{-5.7}$%. With a fixed value of 35% in the analysis, the experimental spectra could not be fit. The value of 35(6)% may be the result of the Pandemonium effect.

In the sum-of-segments spectrum, noticeable features include peaks corresponding to γ rays with a relatively large absolute γ-ray intensity [69]. For example, there is a peak corresponding to the 195.0 keV γ ray.

The β-decay feeding intensity distribution of ^{109}Tc as a function of excitation energy in the daughter nucleus ^{109}Ru is reported in Table V. The β-decay feeding intensity distribution in Table V is an average of the different level schemes assumed for the daughter (Sec. III). The amount of β-decay feeding intensity to known levels is 67.4% and to pseudo levels is 32.6%. The three different sources of uncertainty contributing to the total uncertainty that is reported in Table V were discussed for the case of ^{101}Zr in Sec. IV A. The weighted average of the uncertainty from statistics was 11%. The weighted average of the uncertainty from multiple level schemes was 30%. The uncertainty from the ground-state-to-ground-state transition was determined by comparing the initial number of decaying nuclei between experiment and simulation.

V. NUCLEAR STRUCTURE

The nuclides studied in this work are located in a region characterized by shape coexistence and shape transitions and even axially asymmetric ground-state shapes [88–90]. Therefore, comparing to models can offer insight into the shape of the decaying state of the nuclide. This examination is performed by comparing the experimental results with deformed proton-neutron QRPA calculations.

The theoretical formalism was introduced in Refs. [14–17] and is only briefly summarized here. The method starts with a quasiparticle basis constructed from axially deformed Hartree-Fock (HF) mean-field calculations with density-dependent Skyrme forces and pairing correlations between like nucleons treated in the Bardeen-Cooper-Schrieffer (BCS) framework. The equilibrium deformation is obtained self-consistently as the shape that minimizes the energy. Constrained calculations allow for analyzing the potential energy surfaces and finding various HF energy minima at the corresponding nuclear deformations. A separable spin-isospin residual interaction is then added to the mean field in both particle-hole and particle-particle channels and treated in QRPA to obtain the B(GT) distribution. The calculations of B(GT) within the HF+BCS+QRPA approach are performed for the various equilibrium deformations of each nucleus un-

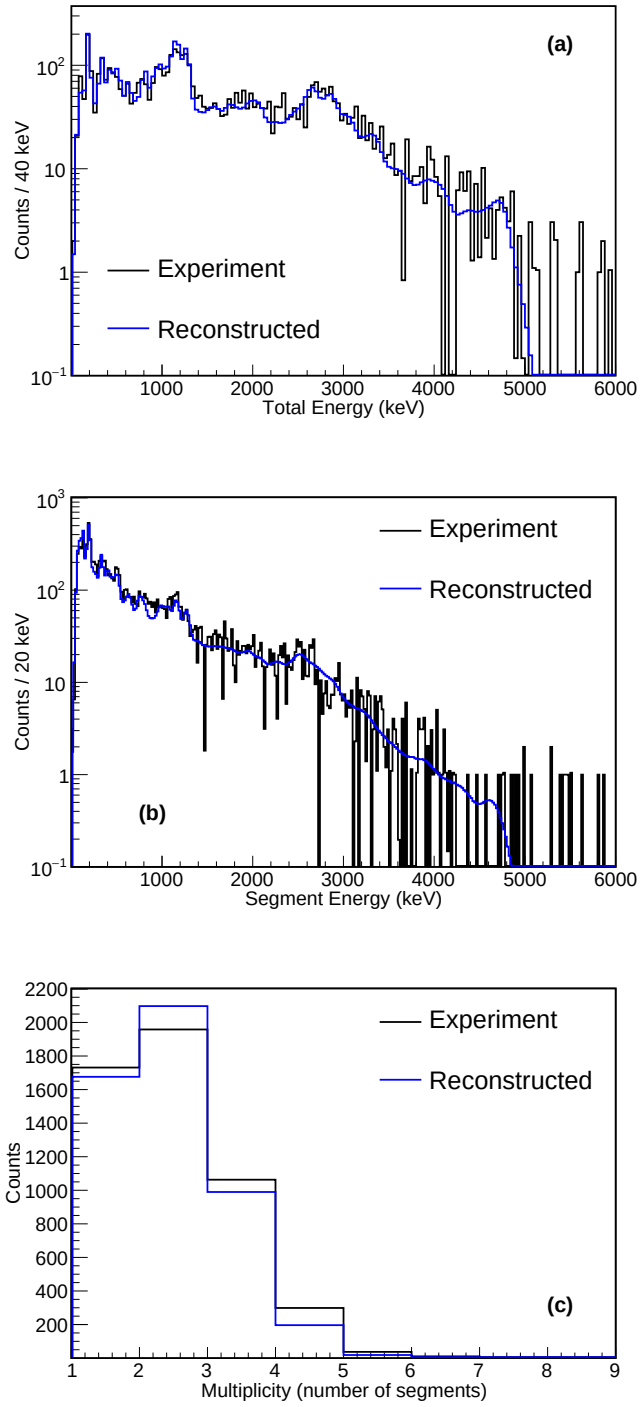

FIG. 3. (Color online) Comparison of experimental (black, solid line) and reconstructed (blue, solid line) spectra from the β decay of ^{109}Tc for the (a) TAS spectrum, (b) sum-of-segments spectrum, and (c) multiplicity spectrum. The experimental spectra were obtained by correlating decay events to ^{109}Tc implantations with a correlation time window of one second. Contamination from random correlations has been subtracted from the experimental spectra. The ground-state-to-ground-state Q value for the β decay of ^{109}Tc is 6456 keV [72].

TABLE V. The β-decay feeding intensity distribution of ^{109}Tc as a function of excitation energy in the daughter nucleus ^{109}Ru. Intensity values below 10^{-4}% are set to 0.

Energy (keV)	Intensity (%)	Error (–)	Error (+)	Energy (keV)	Intensity (%)	Error (–)	Error (+)
0	5.7	5.7	5.8	1830	1.0	0.9	1.2
69	0.35	0.33	0.19	1910	0.50	0.50	0.88
96	0.05	0.05	0.11	1990	2.3	1.1	1.2
132	0.0001	0.0001	0.0002	2080	1.6	1.5	1.5
138	0	0	0	2180	0.5	0.5	1.4
185	3.34	0.32	0.39	2280	0.52	0.52	0.80
191	0	0	0	2380	0.57	0.57	0.97
195	5.26	0.68	0.48	2480	1.24	0.43	0.41
197	0	0	0	2580	0.010	0.010	0.029
230	0.0001	0.0001	0.0002	2680	5.9	2.2	1.1
256	0.0001	0.0001	0.0002	2780	2.3	2.3	3.1
332	3.98	0.50	0.49	2880	2.5	2.2	3.5
405	0.0002	0.0002	0.0005	2980	1.6	1.6	4.0
408	1.55	0.23	0.24	3080	2.6	2.6	1.4
498	0.0001	0.0001	0.0003	3205	0.7	0.7	1.5
515	6.28	0.88	0.88	3355	2.1	1.4	1.0
628	1.73	0.43	0.33	3505	0.39	0.37	0.82
811	4.00	0.51	0.50	3655	0.24	0.24	0.28
995	8.07	0.82	0.82	3805	0.032	0.032	0.094
1159	16.2	1.2	1.2	3955	0.76	0.36	0.77
1268	10.90	0.83	0.80	4105	0.34	0.34	0.27
1350	0.18	0.18	0.52	4255	0.015	0.015	0.045
1430	0.24	0.24	0.31	4405	0.32	0.25	0.50
1510	0.08	0.08	0.24	4570	0.40	0.40	0.33
1590	1.16	1.06	0.44	4750	0.97	0.58	0.73
1670	0.15	0.15	0.38	4930	0.13	0.13	0.12
1750	1.28	1.02	0.63	5110	0	0	0

der the assumption that the parent nucleus and the states fed in the daughter nucleus have the same deformation.

In the following discussion the Skyrme interaction SLy4 [91] is used. It has been widely used in the past with successful results. The results for the β-decay properties in this mass region with other Skyrme forces are qualitatively similar to these although they may differ in details. The sensitivity of the B(GT) distributions to the residual interactions has been studied elsewhere [5, 6, 23] and the parameters used in this work correspond to the most reasonable choices found previously in this mass region. It is worth noting that in general the B(GT) distributions are more sensitive to the nuclear deformation than to the nuclear interactions and this feature was used in the past to learn about the shape of the decaying nucleus [26–32].

For ^{101,102}Zr and ^{109}Tc, the total energy as a function of the quadrupole deformation parameter β_2 shows two minima, oblate and prolate. In the case of the even-even nuclide ^{102}Zr the ground state is found to be prolate at $\beta_2 = 0.373$ and the oblate state appears at $\beta_2 = -0.193$ at about 2 MeV. The odd-A nuclide ^{101}Zr has a prolate ground state ($\beta_2 = 0.362$) and an oblate excited state $\beta_2 = -0.207$ separated by about 2 MeV. Both states are $3/2^+$ neutron states with asymptotic quantum Nilsson numbers given by $[Nn_z\Lambda]K^\pi = \nu[411]3/2^+$ in agreement with experiment and associated to the spherical shell $g_{7/2}$. In the case of ^{109}Tc the ground state is a $\pi[422]5/2^+$ ($g_{9/2}$) state that corresponds to an oblate minimum at $\beta_2 = -0.214$. In addition an isomer prolate state appears at less than 1 MeV with $\pi[303]5/2^-$ ($f_{5/2}$) at $\beta_2 = 0.320$. These states agree well with the observed spectrum in ^{109}Tc that shows a $J^\pi = 5/2^+$ ground state, as well as a $J^\pi = 5/2^-$ excited state at only 7 keV.

In the calculations the $5/2^+$ state would be the oblate state, whereas the $5/2^-$ excited state would be the shape isomer prolate state.

The comparisons between experiment and the HF+BCS+QRPA calculations are shown in Figs. 4, 5, and 6. In these figures, the HF+BCS+QRPA calculations are labeled as "QRPA 1."

A. $^{101}_{40}\mathbf{Zr}_{61} \rightarrow {}^{101}_{41}\mathbf{Nb}_{60}$

Figure 4 shows a comparison of experimental and theoretical cumulative β-decay feeding intensity distributions and cumulative B(GT) distributions for the β decay of ^{101}Zr. Figure 4(a) contains the cumulative β-decay feeding intensity distribution for the present work and QRPA 1 calculations. The QRPA 1 calculations were performed assuming the ground-state shape of ^{101}Zr is oblate ($\beta_2 = -0.207$) and prolate ($\beta_2 = 0.362$). Both shapes have similar half-lives ($T_{1/2} = 3.34$ s for the oblate shape and $T_{1/2} = 3.73$ s for the prolate shape), but different cumulative β-decay feeding intensity distributions. The ground-state-to-ground-state transition in experiment is better reproduced by the prolate shape. Between approximately 500 keV and 2000 keV, the current work is in agreement with the oblate shape. After approximately 2300 keV, the current work is in agreement with both shapes. Both shapes have a relatively large increase in the cumulative β-decay feeding intensity distribution between approximately 1000 keV and 1200 keV that is not observed in the current work. The same situation occurs at approximately 3500 keV. Only the oblate shape has a relatively large increase in the cumulative β-decay feeding intensity distribution at levels near 2000 keV that is observed in experiment.

Figure 4(b) contains the cumulative B(GT) distribution for the present work and QRPA 1. The cumulative B(GT) distributions in Fig. 4(b) correspond to the cumulative β-decay feeding intensity distributions in Fig. 4(a). As with the cumulative β-decay feeding intensity distributions in Fig. 4(a), both shapes have similar half-lives and yet different cumulative B(GT) distributions. Between 0 keV and approximately 1800 keV, the current work is in better agreement with the prolate shape. Between approximately 1800 keV and 3500 keV, the current work is not in agreement with any shape. However, unlike the prolate shape, the oblate shape has an increase in the cumulative B(GT) distribution in this energy region, which is observed in experiment. The cumulative B(GT) distribution in the current work ends approximately in between the cumulative B(GT) distributions for the different shapes. Only the oblate shape has a relatively large increase in the cumulative B(GT) distribution at levels near 2000 keV that is observed in experiment.

The QRPA 1 calculations correspond to pure shape configurations, either oblate or prolate. None of these pure shape configurations reproduce the experimental cumulative β-decay feeding intensity distribution or B(GT) distribution. This may indicate that some type of mixture between these two shapes is necessary to reproduce the result from the current work.

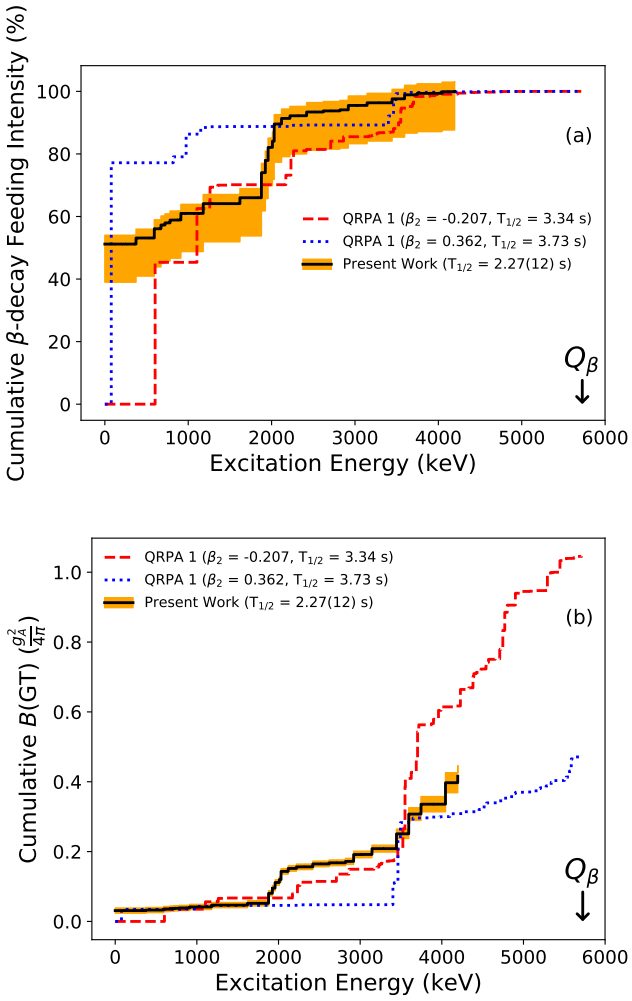

FIG. 4. (Color online) (a) Cumulative β-decay feeding intensity and (b) cumulative B(GT) for the β-decay of ^{101}Zr as a function of excitation energy in the daughter ^{101}Nb. The present work (black, solid line, with uncertainty in orange shading) is compared to QRPA calculations assuming the ground state of the parent is oblate (red, dashed line) and prolate (blue, dotted line). There is an arrow indicating the ground-state-to-ground-state Q value for the β decay of ^{101}Zr at 5726 keV [72]. The half-lives $T_{1/2}$ and quadrupole deformation parameters β_2 are provided in parentheses.

B. $^{102}_{40}\mathbf{Zr}_{62} \rightarrow {}^{102}_{41}\mathbf{Nb}_{61}$

Figure 5 shows a comparison of experimental and theoretical cumulative β-decay feeding intensity distributions and cumulative B(GT) distributions for the β decay of ^{102}Zr. The cumulative β-decay feeding intensity distributions for the present work and QRPA 1 calculations are shown in Fig. 5(a). The QRPA 1 calculations were per-

formed assuming the ground-state shape of ^{102}Zr is oblate ($\beta_2 = -0.193$, $T_{1/2} = 1.43$ s) and prolate ($\beta_2 = 0.373$, $T_{1/2} = 4.01$ s). The transition between the ground state of ^{102}Zr and the β-decaying isomeric state of ^{102}Nb that is extracted in the current work is in between that of the oblate shape and prolate shape. There is good agreement between the current work and the prolate shape between approximately 800 keV and 1500 keV, and there is agreement between the current work and both shapes after approximately 1700 keV. One feature not observed in the current work, but present in both shapes, is the sudden and relatively large increase in the cumulative β-decay feeding intensity distribution between approximately 1800 keV and 2000 keV. The present work has a relatively large β-decay feeding intensity to 599+x keV, which is only seen in the oblate shape.

Figure 5(b) contains the cumulative B(GT) distribution for the present work and QRPA 1. The current work is in agreement with both shapes between 0 keV and approximately 700 keV, and in between both shapes after approximately 1000 keV. The total B(GT) at approximately 3000 keV for the current work is slightly closer to the oblate shape. However, no shape satisfactorily describes the experimental result.

As already mentioned in Sec. V A, the QRPA 1 calculations correspond to pure shape configurations, either oblate or prolate. None of these pure shape configurations reproduce the experimental cumulative β-decay feeding intensity distribution or B(GT) distribution. Similar to ^{101}Zr, this may indicate that some type of mixture between these two shapes is necessary to reproduce the result from the current work.

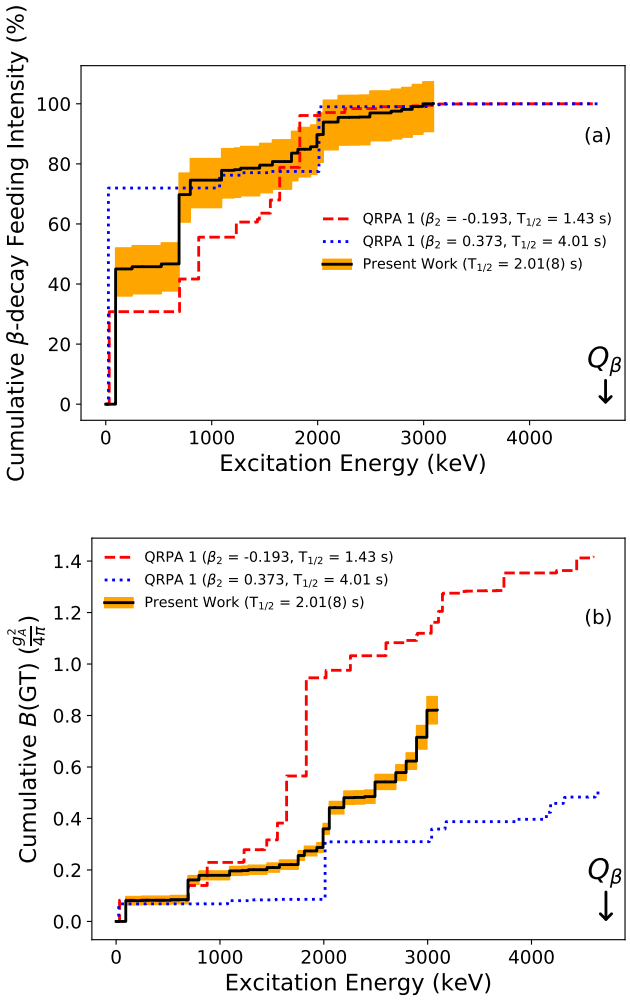

FIG. 5. (Color online) (a) Cumulative β-decay feeding intensity and (b) cumulative B(GT) for the β-decay of ^{102}Zr as a function of excitation energy in the daughter ^{102}Nb. The present work (black, solid line, with uncertainty in orange shading) is compared to QRPA calculations assuming the ground state of the parent is oblate (red, dashed line) and prolate (blue, dotted line). There is an arrow indicating the ground-state-to-ground-state Q value for the β decay of ^{102}Zr at 4717 keV [72]. The half-lives $T_{1/2}$ and quadrupole deformation parameters β_2 are provided in parentheses.

C. $^{109}_{43}\mathbf{Tc}_{66} \rightarrow {}^{109}_{44}\mathbf{Ru}_{65}$

Figure 6 shows a comparison of experimental and theoretical cumulative β-decay feeding intensity distributions and cumulative B(GT) distributions for the β decay of ^{109}Tc. Figure 6(a) contains the cumulative β-decay feeding intensity distribution for the present work and QRPA 1 calculations. The QRPA 1 calculations were performed assuming the ground-state shape of ^{109}Tc is oblate ($\beta_2 = -0.214$, $T_{1/2} = 0.99$ s) and prolate ($\beta_2 = 0.320$, $T_{1/2} = 3.04$ s). Both calculations are in agreement with zero β-decay feeding intensity for the ground-state-to-ground-state transition. Only the oblate shape has any significant β-decay feeding intensity below 2000 keV. Below approximately 1200 keV, the present work and the oblate shape are qualitatively similar. The prolate shape has a sudden and relatively large increase in the cumulative β-decay feeding intensity distribution at approximately 2500 keV, which is not observed in the present work. The current work is not in agreement with the prolate shape until approximately 2500 keV. After approximately 2500 keV, the present work is in agreement with both shapes.

Figure 6(b) contains the cumulative B(GT) distribution for the present work and QRPA 1. Only the oblate shape has any significant B(GT) below 2000 keV. Between approximately 2800 keV and 3400 keV, the present work is in agreement with both shapes. Between approximately 3400 keV and 4800 keV, the present work is in between both shapes. By the energy of the last pseudo level, the total B(GT) for the present work is in agreement with the oblate shape.

For the oblate shape, the increase in β-decay feeding intensity and B(GT) below 1 MeV is mainly due to transitions from neutron states within the $g_{7/2}$, $d_{5/2}$, and $d_{3/2}$ shells to the unpaired proton state $\pi[422]5/2^+$ ($g_{9/2}$). From approximately 2.5 to 3.5 MeV the increase

in β-decay feeding intensity and B(GT) is mainly due to transitions connecting neutron states from $g_{7/2}$, $d_{5/2}$, $s_{1/2}$, and $d_{3/2}$ shells to other proton states of the $g_{9/2}$ shell different from the unpaired state.

For the prolate shape, there is minimal β-decay feeding intensity and B(GT) below approximately 2.5 MeV because the unpaired proton $\pi[303]5/2^-$ ($f_{5/2}$) of negative parity is not connected by allowed Gamow-Teller transitions with the neutron states around the Fermi level ($g_{7/2}$, $d_{5/2}$, $s_{1/2}$, $d_{3/2}$), which are positive-parity states. Only above approximately 2.5 MeV (about twice the pairing gap) do new transitions occur with the odd proton as a spectator, leading to three quasiparticle states of one unpaired neutron and two unpaired protons. The increase in β-decay feeding intensity and B(GT) at approximately 2.5 MeV corresponds to neutrons in the $\nu[413]5/2^+$ ($d_{5/2}$) orbital converted into protons in the $\pi[413]7/2^+$ ($g_{9/2}$) orbital.

The cumulative β-decay feeding intensity distribution for the oblate shape better describes the current work. In addition, the half-lives for the present work and the oblate shape are in agreement. The total B(GT) for the present work and the oblate shape are in agreement below the one-neutron separation energy of the daughter. All these facts suggest a dominant oblate deformation for ^{109}Tc, in agreement with the $J^\pi = 5/2^+$ of the ground state. In Ref. [92], β- and γ-coincidence spectroscopy of the nearby technetium isotope ^{111}Tc provided evidence of oblate deformation for that nucleus. Therefore, the current work is in agreement with Ref. [92] in terms of a nearby technetium isotope in the same mass region having a similar deformation.

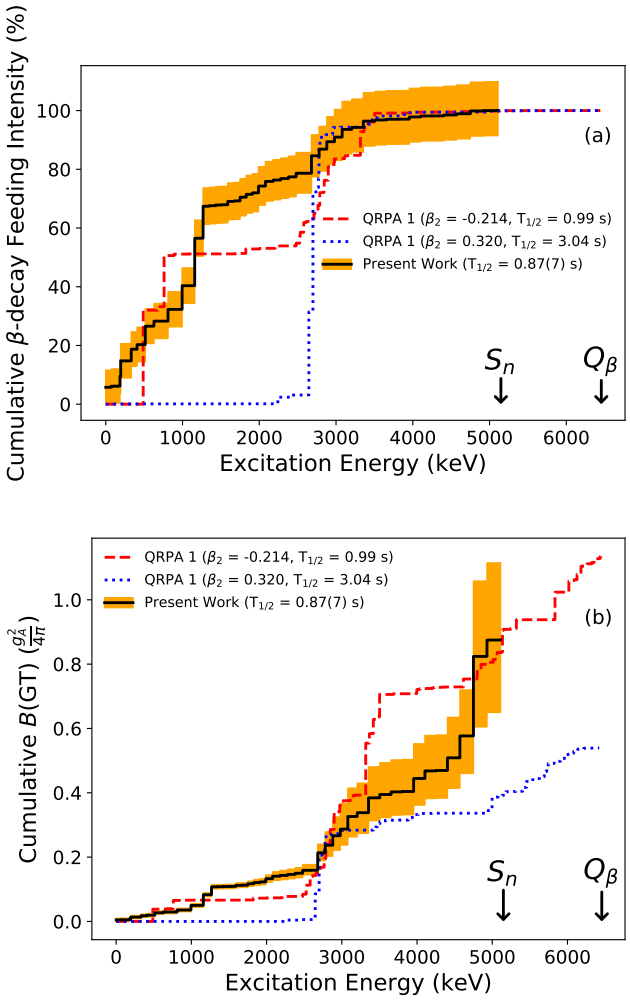

FIG. 6. (Color online) (a) Cumulative β-decay feeding intensity and (b) cumulative B(GT) for the β-decay of ^{109}Tc as a function of excitation energy in the daughter ^{109}Ru. The present work (black, solid line, with uncertainty in orange shading) is compared to QRPA calculations assuming the ground state of the parent is oblate (red, dashed line) and prolate (blue, dotted line). There is an arrow indicating the ground-state-to-ground-state Q value for the β decay of ^{109}Tc at 6456 keV [72]. There is an arrow indicating the one-neutron separation energy S_n of the daughter ^{109}Ru at 5148 keV [72]. The half-lives $T_{1/2}$ and quadrupole deformation parameters β_2 are provided in parentheses.

VI. NUCLEAR ASTROPHYSICS

In this section, the experimental results are compared to QRPA models that are commonly used to provide β-decay properties in r-process network calculations. These comparisons are shown in Figs. 7, 8, and 9. Two different QRPA models are used in these comparisons.

One model is labeled as "QRPA 2" in Figs. 7, 8, and 9. Within QRPA 2, the large-scale calculation of β-decay half-lives was performed in two steps: (i) determination of the ground state of the parent nucleus, (ii) calculation of transition energies and strengths in the β decays of neutron-rich nuclei. The ground state of a nucleus was obtained within the fully microscopic theoretical framework based on the relativistic nuclear energy density functional (RNEDF). The nuclear ground state properties are described using the relativistic Hartree-Bogoliubov (RHB) model, which is able to properly treat the pairing effects in open shell nuclei. The actual calculation was performed using the D3C* interaction [93], which includes momentum-dependent terms in the underlying Lagrangian.

The nuclear response is obtained using the proton-neutron relativistic quasiparticle random-phase approximation (pn-RQRPA). The identical D3C* interaction is used at the RQRPA level as at the RHB level, that is, the model is fully self-consistent in both the particle-hole and particle-particle channels. By solving the pn-RQRPA matrix equations, energies and amplitudes are obtained from which the nuclear response to a particular operator can be determined. The details of the calculation, together with exact expressions for the matrix elements involved, can be found in Ref. [94].

QRPA 2 is based on a relativistic model, is fully self-consistent, and includes first-forbidden transitions, but

assumes spherically symmetric nuclei. Therefore, there is an implicit $\beta_2 = 0$ for QRPA 2.

Another model is labeled as "QRPA 3" in Figs. 7, 8, and 9. The QRPA 3 calculations are done as described in Refs. [95, 96]. As stated in Ref. [96], the recently enhanced mass model FRDM (2012) and more accurate ground-state shapes and corresponding Q_β values are used.

A. $^{101}_{40}\mathbf{Zr}_{61} \rightarrow {}^{101}_{41}\mathbf{Nb}_{60}$

Figure 7(a) contains the cumulative β-decay feeding intensity distribution for the present work, QRPA 2, and QRPA 3. None of these QRPA calculations reproduce the ground-state-to-ground-state transition from the current work. None of these calculations reproduce the structure in the cumulative β-decay feeding intensity distribution from the current work. The half-life from QRPA 3 is longer than the half-life extracted in the current work by more than a factor of ten.

Figure 7(b) contains the cumulative B(GT) distribution for the present work, QRPA 2, and QRPA 3. The cumulative B(GT) distributions in Fig. 7(b) correspond to the cumulative β-decay feeding intensity distributions in Fig. 7(a). The cumulative B(GT) distribution from the current work is not in agreement with QRPA 2 or QRPA 3 at any energy. Note that the quadrupole deformation parameter used in QRPA 3 is $\beta_2 = 0.376$. This is similar to the value used in QRPA 1 ($\beta_2 = 0.362$). In addition, the cumulative B(GT) distributions for these prolate shapes are qualitatively similar. For example, both calculations have a small cumulative B(GT) at low energies, and then a relatively large increase in the cumulative B(GT) at approximately 3500 keV. The total B(GT) within the ground-state-to-ground-state Q value is similar for both calculations. However, the half-lives for the prolate calculations (3.73 s and 37.48 s) are different. In addition, the cumulative β-decay feeding intensity distributions for the prolate shapes are markedly different.

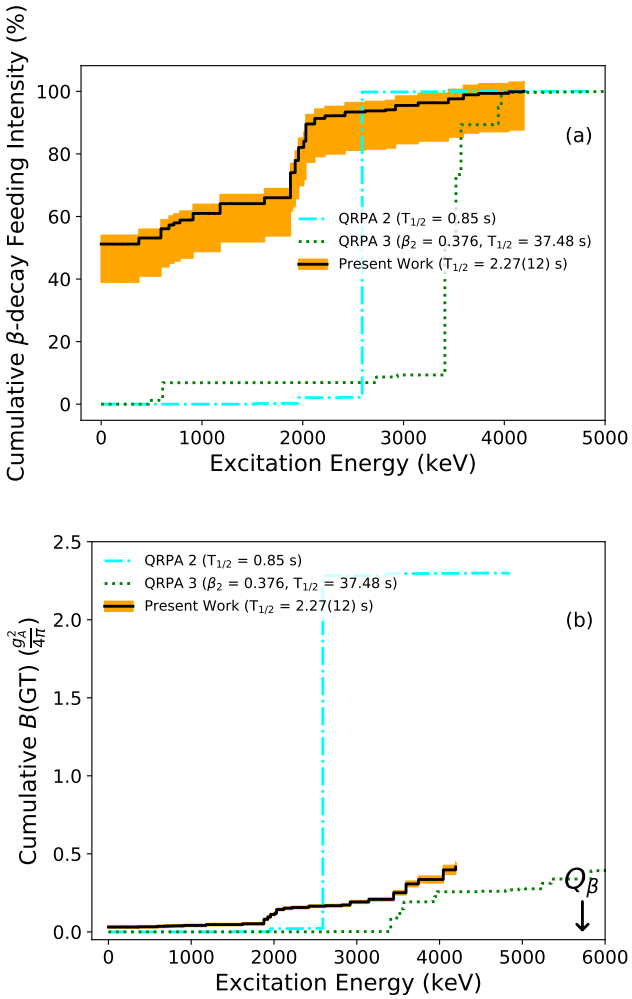

FIG. 7. (Color online) (a) Cumulative β-decay feeding intensity and (b) cumulative B(GT) for the β-decay of ^{101}Zr as a function of excitation energy in the daughter ^{101}Nb. The present work (black, solid line, with uncertainty in orange shading) is compared to QRPA 2 (cyan, dash-dotted line) and QRPA 3 (green, dotted line). There is an arrow indicating the ground-state-to-ground-state Q value for the β decay of ^{101}Zr at 5726 keV [72]. The half-lives $T_{1/2}$ and quadrupole deformation parameters β_2 are provided in parentheses.

B. $^{102}_{40}\mathbf{Zr}_{62} \rightarrow {}^{102}_{41}\mathbf{Nb}_{61}$

Figure 8(a) contains the cumulative β-decay feeding intensity distribution for the present work, QRPA 2, and QRPA 3. The transition between the ground state of ^{102}Zr and the β-decaying isomeric state of ^{102}Nb that is extracted in the current work is not reproduced by either calculation. Only QRPA 3 has a relatively large β-decay feeding intensity to a level with very low energy (less than 100 keV). Almost 100% of the β-decay feeding intensity goes to a level at approximately 1300 keV in QRPA 2. Levels between approximately 1500 keV and 2000 keV collectively receive most of the β-decay feeding intensity in QRPA 3. None of these calculations reproduce the relatively large increase in the cumulative β-decay feeding intensity distribution at 599+x keV that is observed in the current work.

Figure 8(b) contains the cumulative B(GT) distribution for the present work, QRPA 2, and QRPA 3. The cumulative B(GT) distribution from the current work is not in agreement with either QRPA calculation at any energy. In this QRPA calculation, the quadrupole deformation parameter is $\beta_2 = 0.376$. The QRPA 1 calculation uses a similar value for the prolate shape of $\beta_2 = 0.373$. The cumulative B(GT) distributions for these prolate shapes are qualitatively similar between 0 keV and 4000 keV. The total B(GT) from 0 keV to 4000 keV is similar for both calculations. In addition, the cumulative B(GT) distributions from both calculations are

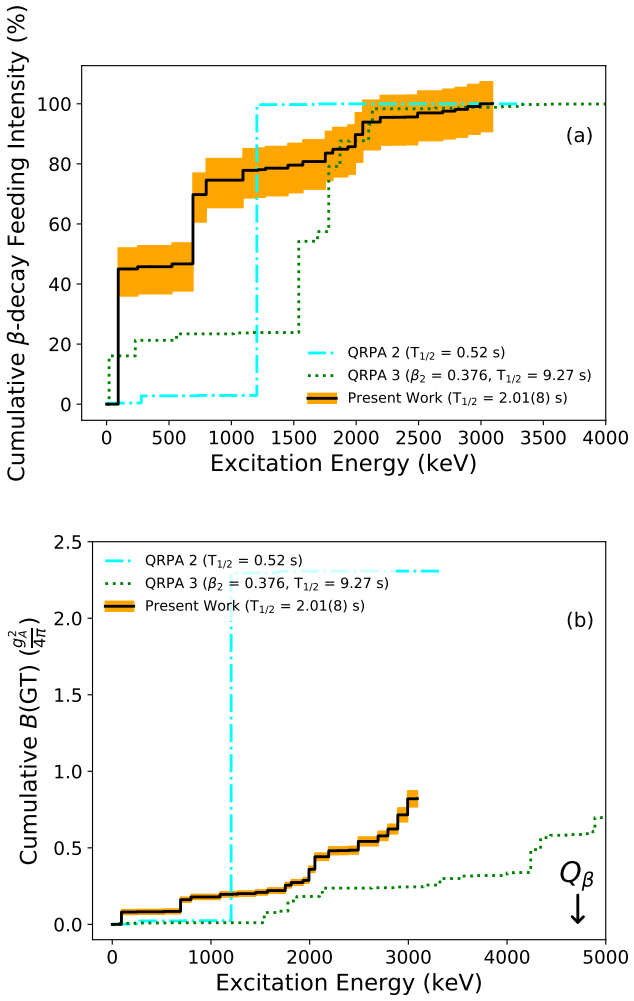

FIG. 8. (Color online) (a) Cumulative β-decay feeding intensity and (b) cumulative B(GT) for the β-decay of ^{102}Zr as a function of excitation energy in the daughter ^{102}Nb. The present work (black, solid line, with uncertainty in orange shading) is compared to QRPA 2 (cyan, dash-dotted line) and QRPA 3 (green, dotted line). There is an arrow indicating the ground-state-to-ground-state Q value for the β decay of ^{102}Zr at 4717 keV [72]. The half-lives $T_{1/2}$ and quadrupole deformation parameters β_2 are provided in parentheses.

always less than experiment. However, the half-lives for the prolate calculations (4.01 s and 9.27 s) are different.

C. $^{109}_{43}$Tc$_{66} \rightarrow ^{109}_{44}Ru_{65}$

Figure 9(a) contains the cumulative β-decay feeding intensity distribution for the present work, QRPA 2, and QRPA 3. The calculated ground-state shape in the FRDM model is axially asymmetric [89] but the QRPA 3 computer code cannot accommodate such shapes. Therefore the QRPA 3 calculations were performed assuming the ground-state shape of ^{109}Tc is either oblate ($\beta_2 = -0.2481$) or prolate ($\beta_2 = 0.309$), that is for the constrained minima on the oblate and prolate axes. All calculations are in agreement with zero β-decay feeding intensity for the ground-state-to-ground-state transition. All calculations have a sudden and relatively large increase in the cumulative β-decay feeding intensity distribution. However, the cumulative β-decay feeding intensity distribution for the present work shows more fragmentation and a gradual increase throughout the entire energy range.

Figure 9(b) contains the cumulative B(GT) distribution for the present work, QRPA 2, and QRPA 3. The cumulative B(GT) distribution from the current work and QRPA 3 are rarely in agreement for any energy. Between 0 keV and the one-neutron separation energy of the daughter, the present work is in between both shapes. At the one-neutron separation energy of the daughter, the total B(GT) for the present work is in agreement with the oblate shape.

There are many similarities in the calculations from QRPA 1 and QRPA 3. The quadrupole deformation parameters of the oblate shapes ($\beta_2 = -0.214$ and $\beta_2 = -0.2481$) are close in value, as well as the prolate shapes ($\beta_2 = 0.320$ and $\beta_2 = 0.309$). The half-lives of the oblate shapes ($T_{1/2} = 0.99$ s and $T_{1/2} = 0.32$ s) are similar, and the same is true for the prolate shapes ($T_{1/2} = 3.04$ s and $T_{1/2} = 4.50$ s). The half-lives of the oblate shapes are shorter than those of the prolate shapes.

The oblate shapes have a relatively large increase in the cumulative β-decay feeding intensity distribution at low energies. The increase occurs at similar energies for the oblate shapes. In QRPA 1, the increase occurs at approximately 400 keV. In QRPA 3, the increase occurs at approximately 300 keV. The increase is larger in the QRPA 3 calculation. The prolate shapes have a small cumulative β-decay feeding intensity at low energies, and then a sudden and relatively large increase in the cumulative β-decay feeding intensity distribution at higher energies. The increase occurs at similar energies for the prolate shapes. In QRPA 1, the increase occurs at approximately 2500 keV. In QRPA 3, the increase occurs at approximately 3000 keV. The cumulative B(GT) distributions for the prolate shapes are less than the current work.

VII. CONCLUSIONS

In the first-ever application of the total absorption spectroscopy technique with a fast beam produced via projectile fragmentation, the β-decay feeding intensity distributions and B(GT) distributions were extracted for ^{101}Zr, ^{102}Zr, and ^{109}Tc. The experiment was performed at the National Superconducting Cyclotron Laboratory using the Summing NaI(Tl) (SuN) detector. The extracted distributions were compared to calculated results from three different quasiparticle random-phase approximation (QRPA) models to learn about the ground-state shape of the parent nucleus and test models commonly

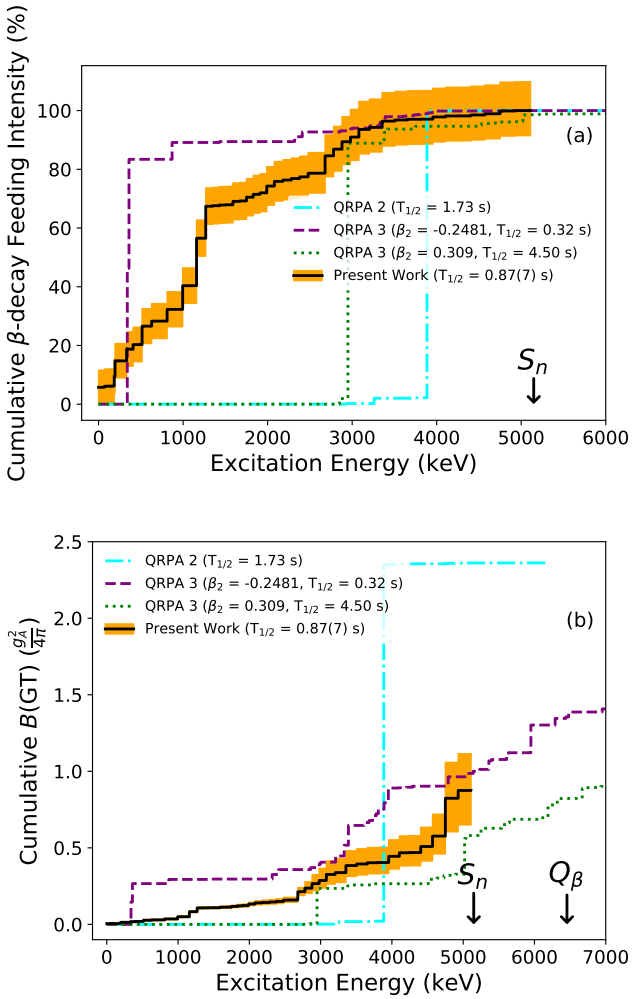

FIG. 9. (Color online) (a) Cumulative β-decay feeding intensity and (b) cumulative B(GT) for the β-decay of ^{109}Tc as a function of excitation energy in the daughter ^{109}Ru. The present work (black, solid line, with uncertainty in orange shading) is compared to QRPA 2 (cyan, dash-dotted line) and QRPA 3 (green, dotted line and purple, dashed line). There is an arrow indicating the ground-state-to-ground-state Q value for the β decay of ^{109}Tc at 6456 keV [72]. There is an arrow indicating the one-neutron separation energy S_n of the daughter ^{109}Ru at 5148 keV [72]. The half-lives $T_{1/2}$ and quadrupole deformation parameters β_2 are provided in parentheses.

used to provide β-decay properties in r-process network calculations. For ^{101}Zr and ^{102}Zr, calculations assuming a pure shape configuration (oblate or prolate) were not able to reproduce the extracted distributions. These results may indicate that some type of mixture between oblate and prolate shapes occurs in actual nuclei, which is not yet taken into account in model calculations. For ^{109}Tc, a comparison of the extracted distributions with QRPA calculations suggests a dominant oblate configuration. Comparing the extracted distributions to the models used in r-process network calculations shows the importance of making comparisons between the experimental and theoretical distributions, rather than integral quantities such as β-decay half-lives and β-delayed neutron emission probabilities, as close to the r-process path as possible.

ACKNOWLEDGMENTS

A. A. acknowledges support from the Spanish Ministerio de Economía y Competitividad under Grant Nos. FPA2011-24553, FPA2014-52823-C2-1-P, FPA2017-83946-C2-1-P and the program Severo Ochoa (SEV-2014-0398). P. S. acknowledges support from MCIU/AEI/FEDER,UE (Spain) under Contract No. PGC2018-093636-B-I00. S. V. acknowledges support from Czech Science Foundation Project No. 19-14048 and the Charles University Project No. UNCE/SCI/013. This work was supported by the National Science Foundation under Grants No. PHY 1565546 (NSCL), No. PHY 1430152 (JINA-CEE), and No. PHY 1350234 (CAREER). This material is based upon work supported by the Department of Energy National Nuclear Security Administration through the Nuclear Science and Security Consortium under Award Number(s) DE-NA0003180 and/or DE-NA0000979.

[1] M. Arnould, S. Goriely, and K. Takahashi, Physics Reports **450**, 97 (2007).
[2] D. Kasen, B. Metzger, J. Barnes, E. Quataert, and E. Ramirez-Ruiz, Nature **551**, 80 (2017).
[3] M. R. Mumpower, R. Surman, G. C. McLaughlin, and A. Aprahamian, Progress in Particle and Nuclear Physics **86**, 86 (2016).
[4] D. Watson, C. J. Hansen, J. Selsing, A. Koch, D. B. Malesani, A. C. Andersen, J. P. U. Fynbo, A. Arcones, A. Bauswein, S. Covino, A. Grado, K. E. Heintz, L. Hunt, C. Kouveliotou, G. Leloudas, A. J. Levan, P. Mazzali, and E. Pian, Nature **574**, 497 (2019).
[5] P. Sarriguren and J. Pereira, Phys. Rev. C **81**, 064314 (2010).
[6] P. Sarriguren, A. Algora, and J. Pereira, Phys. Rev. C **89**, 034311 (2014).
[7] J. Krumlinde and P. Möller, Nuclear Physics A **417**, 419 (1984).
[8] B. Rubio and W. Gelletly, "Beta Decay of Exotic Nuclei," in *The Euroschool Lectures on Physics with Exotic Beams, Vol. III*, edited by J. S. Al-Khalili and E. Roeckl (Springer Berlin Heidelberg, Berlin, Heidelberg, 2009)

pp. 99–151.
[9] Y. Fujita, B. Rubio, and W. Gelletly, Progress in Particle and Nuclear Physics **66**, 549 (2011).
[10] P. Urkedal, X. Z. Zhang, and I. Hamamoto, Phys. Rev. C **64**, 054304 (2001).
[11] J. L. Wood, K. Heyde, W. Nazarewicz, M. Huyse, and P. Van Duppen, Physics Reports **215**, 101 (1992).
[12] I. Hamamoto and X. Z. Zhang, Zeitschrift für Physik A Hadrons and Nuclei **353**, 145 (1995).
[13] F. Frisk, I. Hamamoto, and X. Z. Zhang, Phys. Rev. C **52**, 2468 (1995).
[14] P. Sarriguren, E. Moya de Guerra, A. Escuderos, and A. C. Carrizo, Nuclear Physics A **635**, 55 (1998).
[15] P. Sarriguren, E. Moya de Guerra, and A. Escuderos, Nuclear Physics A **658**, 13 (1999).
[16] P. Sarriguren, E. Moya de Guerra, and A. Escuderos, Nuclear Physics A **691**, 631 (2001).
[17] P. Sarriguren, E. Moya de Guerra, and A. Escuderos, Phys. Rev. C **64**, 064306 (2001).
[18] P. Sarriguren, O. Moreno, R. Álvarez-Rodríguez, and E. Moya de Guerra, Phys. Rev. C **72**, 054317 (2005).
[19] O. Moreno, P. Sarriguren, R. Álvarez-Rodríguez, and E. Moya de Guerra, Phys. Rev. C **73**, 054302 (2006).
[20] O. Moreno, R. Álvarez-Rodríguez, P. Sarriguren, E. Moya de Guerra, J. M. Udías, and J. R. Vignote, Phys. Rev. C **74**, 054308 (2006).
[21] P. Sarriguren, Phys. Rev. C **79**, 044315 (2009).
[22] J. M. Boillos and P. Sarriguren, Phys. Rev. C **91**, 034311 (2015).
[23] P. Sarriguren, Phys. Rev. C **91**, 044304 (2015).
[24] P. Sarriguren, Phys. Rev. C **95**, 014304 (2017).
[25] P. Sarriguren, A. Algora, and G. Kiss, Phys. Rev. C **98**, 024311 (2018).
[26] E. Poirier, F. Maréchal, Ph. Dessagne, A. Algora, M. J. G. Borge, D. Cano-Ott, J. C. Caspar, S. Courtin, J. Devin, L. M. Fraile, W. Gelletly, G. Heitz, A. Jungclaus, G. Le Scornet, Ch. Miehé, E. Nácher, B. Rubio, P. Sarriguren, J. L. Tain, O. Tengblad, and C. Weber (the ISOLDE Collaboration), Phys. Rev. C **69**, 034307 (2004).
[27] E. Nácher, A. Algora, B. Rubio, J. L. Taín, D. Cano-Ott, S. Courtin, Ph. Dessagne, F. Maréchal, Ch. Miehé, E. Poirier, M. J. G. Borge, D. Escrig, A. Jungclaus, P. Sarriguren, O. Tengblad, W. Gelletly, L. M. Fraile, and G. Le Scornet, Phys. Rev. Lett. **92**, 232501 (2004).
[28] D. Jordan, A. Algora, J. L. Taín, B. Rubio, J. Agramunt, A. B. Perez-Cerdan, F. Molina, L. Caballero, E. Nácher, A. Krasznahorkay, M. D. Hunyadi, J. Gulyás, A. Vitéz, M. Csatlós, L. Csige, J. Äysto, H. Penttilä, I. D. Moore, T. Eronen, A. Jokinen, A. Nieminen, J. Hakala, P. Karvonen, A. Kankainen, A. Saastamoinen, J. Rissanen, T. Kessler, C. Weber, J. Ronkainen, S. Rahaman, V. Elomaa, U. Hager, S. Rinta-Antila, T. Sonoda, K. Burkard, W. Hüller, L. Batist, W. Gelletly, A. L. Nichols, T. Yoshida, A. A. Sonzogni, K. Peräjärvi, A. Petrovici, K. W. Schmid, and A. Faessler, Phys. Rev. C **87**, 044318 (2013).
[29] A. B. Pérez-Cerdán, B. Rubio, W. Gelletly, A. Algora, J. Agramunt, E. Nácher, J. L. Taín, P. Sarriguren, L. M. Fraile, M. J. G. Borge, L. Caballero, Ph. Dessagne, A. Jungclaus, G. Heitz, F. Marechal, E. Poirier, M. D. Salsac, and O. Tengblad, Phys. Rev. C **88**, 014324 (2013).
[30] M. E. Estévez Aguado, A. Algora, J. Agramunt, B. Rubio, J. L. Taín, D. Jordán, L. M. Fraile, W. Gelletly, A. Frank, M. Csatlós, L. Csige, Zs. Dombrádi, A. Krasznahorkay, E. Nácher, P. Sarriguren, M. J. G. Borge, J. A. Briz, O. Tengblad, F. Molina, O. Moreno, M. Kowalska, V. N. Fedosseev, B. A. Marsh, D. V. Fedorov, P. L. Molkanov, A. N. Andreyev, M. D. Seliverstov, K. Burkard, and W. Hüller, Phys. Rev. C **92**, 044321 (2015).
[31] J. A. Briz, E. Nácher, M. J. G. Borge, A. Algora, B. Rubio, Ph. Dessagne, A. Maira, D. Cano-Ott, S. Courtin, D. Escrig, L. M. Fraile, W. Gelletly, A. Jungclaus, G. Le Scornet, F. Maréchal, Ch. Miehé, E. Poirier, A. Poves, P. Sarriguren, J. L. Taín, and O. Tengblad, Phys. Rev. C **92**, 054326 (2015).
[32] S. Rice, A. Algora, J. L. Tain, E. Valencia, J. Agramunt, B. Rubio, W. Gelletly, P. H. Regan, A.-A. Zakari-Issoufou, M. Fallot, A. Porta, J. Rissanen, T. Eronen, J. Äystö, L. Batist, M. Bowry, V. M. Bui, R. Caballero-Folch, D. Cano-Ott, V.-V. Elomaa, E. Estevez, G. F. Farrelly, A. R. Garcia, B. Gomez-Hornillos, V. Gorlychev, J. Hakala, M. D. Jordan, A. Jokinen, V. S. Kolhinen, F. G. Kondev, T. Martínez, P. Mason, E. Mendoza, I. Moore, H. Penttilä, Zs. Podolyák, M. Reponen, V. Sonnenschein, A. A. Sonzogni, and P. Sarriguren, Phys. Rev. C **96**, 014320 (2017).
[33] V. Guadilla, A. Algora, J. L. Tain, J. Agramunt, J. Äystö, J. A. Briz, A. Cucoanes, T. Eronen, M. Estienne, M. Fallot, L. M. Fraile, E. Ganioğlu, W. Gelletly, D. Gorelov, J. Hakala, A. Jokinen, D. Jordan, A. Kankainen, V. Kolhinen, J. Koponen, M. Lebois, L. Le Meur, T. Martinez, M. Monserrate, A. Montaner-Pizá, I. Moore, E. Nácher, S. E. A. Orrigo, H. Penttilä, I. Pohjalainen, A. Porta, J. Reinikainen, M. Reponen, S. Rinta-Antila, B. Rubio, K. Rytkönen, P. Sarriguren, T. Shiba, V. Sonnenschein, A. A. Sonzogni, E. Valencia, V. Vedia, A. Voss, J. N. Wilson, and A.-A. Zakari-Issoufou, Phys. Rev. C **100**, 024311 (2019).
[34] J. C. Hardy, L. C. Carraz, B. Jonson, and P. G. Hansen, Physics Letters B **71**, 307 (1977).
[35] V. Guadilla, A. Algora, J. L. Tain, J. Agramunt, D. Jordan, A. Montaner-Pizá, S. E. A. Orrigo, B. Rubio, E. Valencia, J. Suhonen, O. Civitarese, J. Äystö, J. A. Briz, A. Cucoanes, T. Eronen, M. Estienne, M. Fallot, L. M. Fraile, E. Ganioğlu, W. Gelletly, D. Gorelov, J. Hakala, A. Jokinen, A. Kankainen, V. Kolhinen, J. Koponen, M. Lebois, T. Martinez, M. Monserrate, I. Moore, E. Nácher, H. Penttilä, I. Pohjalainen, A. Porta, J. Reinikainen, M. Reponen, S. Rinta-Antila, K. Rytkönen, T. Shiba, V. Sonnenschein, A. A. Sonzogni, V. Vedia, A. Voss, J. N. Wilson, and A.-A. Zakari-Issoufou, Phys. Rev. C **96**, 014319 (2017).
[36] A. Algora, D. Jordan, J. L. Taín, B. Rubio, J. Agramunt, A. B. Perez-Cerdan, F. Molina, L. Caballero, E. Nácher, A. Krasznahorkay, M. D. Hunyadi, J. Gulyás, A. Vitéz, M. Csatlós, L. Csige, J. Äysto, H. Penttilä, I. D. Moore, T. Eronen, A. Jokinen, A. Nieminen, J. Hakala, P. Karvonen, A. Kankainen, A. Saastamoinen, J. Rissanen, T. Kessler, C. Weber, J. Ronkainen, S. Rahaman, V. Elomaa, S. Rinta-Antila, U. Hager, T. Sonoda, K. Burkard, W. Hüller, L. Batist, W. Gelletly, A. L. Nichols, T. Yoshida, A. A. Sonzogni, and K. Peräjärvi, Phys. Rev. Lett. **105**, 202501 (2010).

[37] M. Fallot, S. Cormon, M. Estienne, A. Algora, V. M. Bui, A. Cucoanes, M. Elnimr, L. Giot, D. Jordan, J. Martino, A. Onillon, A. Porta, G. Pronost, A. Remoto, J. L. Taín, F. Yermia, and A.-A. Zakari-Issoufou, Phys. Rev. Lett. **109**, 202504 (2012).

[38] P. Dimitriou and A. L. Nichols, "Total Absorption Gamma-ray Spectroscopy for Decay Heat Calculations and Other Applications," (2015).

[39] G. Mention, M. Fechner, Th. Lasserre, Th. A. Mueller, D. Lhuillier, M. Cribier, and A. Letourneau, Phys. Rev. D **83**, 073006 (2011).

[40] M. Fallot, Nuclear Data Sheets **120**, 137 (2014).

[41] E. Christensen, P. Huber, P. Jaffke, and T. E. Shea, Phys. Rev. Lett. **113**, 042503 (2014).

[42] P. Jaffke and P. Huber, Phys. Rev. Applied **8**, 034005 (2017).

[43] A. C. Dombos, A. Spyrou, F. Naqvi, S. J. Quinn, S. N. Liddick, A. Algora, T. Baumann, J. Brett, B. P. Crider, P. A. DeYoung, T. Ginter, J. Gombas, E. Kwan, S. Lyons, W.-J. Ong, A. Palmisano, J. Pereira, C. J. Prokop, D. P. Scriven, A. Simon, M. K. Smith, and C. S. Sumithrarachchi, Phys. Rev. C **99**, 015802 (2019).

[44] D. J. Morrissey, B. M. Sherrill, M. Steiner, A. Stolz, and I. Wiedenhoever, Nuclear Instruments and Methods in Physics Research Section B: Beam Interactions with Materials and Atoms **204**, 90 (2003), 14th International Conference on Electromagnetic Isotope Separators and Techniques Related to their Applications.

[45] C. J. Prokop, S. N. Liddick, B. L. Abromeit, A. T. Chemey, N. R. Larson, S. Suchyta, and J. R. Tompkins, Nuclear Instruments and Methods in Physics Research Section A: Accelerators, Spectrometers, Detectors and Associated Equipment **741**, 163 (2014).

[46] J. I. Prisciandaro, A. C. Morton, and P. F. Mantica, Nuclear Instruments and Methods in Physics Research Section A: Accelerators, Spectrometers, Detectors and Associated Equipment **505**, 140 (2003), proceedings of the tenth Symposium on Radiation Measurements and Applications.

[47] A. Simon, S. J. Quinn, A. Spyrou, A. Battaglia, I. Beskin, A. Best, B. Bucher, M. Couder, P. A. DeYoung, X. Fang, J. Görres, A. Kontos, Q. Li, S. N. Liddick, A. Long, S. Lyons, K. Padmanabhan, J. Peace, A. Roberts, D. Robertson, K. Smith, M. K. Smith, E. Stech, B. Stefanek, W. P. Tan, X. D. Tang, and M. Wiescher, Nuclear Instruments and Methods in Physics Research Section A: Accelerators, Spectrometers, Detectors and Associated Equipment **703**, 16 (2013).

[48] D. Cano-Ott, J. L. Tain, A. Gadea, B. Rubio, L. Batist, M. Karny, and E. Roeckl, Nuclear Instruments and Methods in Physics Research Section A: Accelerators, Spectrometers, Detectors and Associated Equipment **430**, 333 (1999).

[49] S. Agostinelli, J. Allison, K. Amako, J. Apostolakis, H. Araujo, P. Arce, M. Asai, D. Axen, S. Banerjee, G. Barrand, F. Behner, L. Bellagamba, J. Boudreau, L. Broglia, A. Brunengo, H. Burkhardt, S. Chauvie, J. Chuma, R. Chytracek, G. Cooperman, G. Cosmo, P. Degtyarenko, A. Dell'Acqua, G. Depaola, D. Dietrich, R. Enami, A. Feliciello, C. Ferguson, H. Fesefeldt, G. Folger, F. Foppiano, A. Forti, S. Garelli, S. Giani, R. Giannitrapani, D. Gibin, J. J. G. Cadenas, I. González, G. G. Abril, G. Greeniaus, W. Greiner, V. Grichine, A. Grossheim, S. Guatelli, P. Gumplinger, R. Hamatsu, K. Hashimoto, H. Hasui, A. Heikkinen, A. Howard, V. Ivanchenko, A. Johnson, F. W. Jones, J. Kallenbach, N. Kanaya, M. Kawabata, Y. Kawabata, M. Kawaguti, S. Kelner, P. Kent, A. Kimura, T. Kodama, R. Kokoulin, M. Kossov, H. Kurashige, E. Lamanna, T. Lampén, V. Lara, V. Lefebure, F. Lei, M. Liendl, W. Lockman, F. Longo, S. Magni, M. Maire, E. Medernach, K. Minamimoto, P. M. de Freitas, Y. Morita, K. Murakami, M. Nagamatu, R. Nartallo, P. Nieminen, T. Nishimura, K. Ohtsubo, M. Okamura, S. O'Neale, Y. Oohata, K. Paech, J. Perl, A. Pfeiffer, M. G. Pia, F. Ranjard, A. Rybin, S. Sadilov, E. D. Salvo, G. Santin, T. Sasaki, N. Savvas, Y. Sawada, S. Scherer, S. Sei, V. Sirotenko, D. Smith, N. Starkov, H. Stoecker, J. Sulkimo, M. Takahata, S. Tanaka, E. Tcherniaev, E. S. Tehrani, M. Tropeano, P. Truscott, H. Uno, L. Urban, P. Urban, M. Verderi, A. Walkden, W. Wander, H. Weber, J. P. Wellisch, T. Wenaus, D. C. Williams, D. Wright, T. Yamada, H. Yoshida, and D. Zschiesche, Nuclear Instruments and Methods in Physics Research Section A: Accelerators, Spectrometers, Detectors and Associated Equipment **506**, 250 (2003).

[50] P. Venkataramaiah, K. Gopala, A. Basavaraju, S. S. Suryanarayana, and H. Sanjeeviah, Journal of Physics G: Nuclear Physics **11**, 359 (1985).

[51] R. Capote, M. Herman, P. Obložinský, P. G. Young, S. Goriely, T. Belgya, A. V. Ignatyuk, A. J. Koning, S. Hilaire, V. A. Plujko, M. Avrigeanu, O. Bersillon, M. B. Chadwick, T. Fukahori, Zhigang Ge, Yinlu Han, S. Kailas, J. Kopecky, V. M. Maslov, G. Reffo, M. Sin, E. Sh. Soukhovitskii, and P. Talou, Nuclear Data Sheets **110**, 3107 (2009), special Issue on Nuclear Reaction Data.

[52] J. Tuli, Nuclear Instruments and Methods in Physics Research Section A: Accelerators, Spectrometers, Detectors and Associated Equipment **369**, 506 (1996).

[53] B. C. Rasco, A. Fijałkowska, M. Karny, K. P. Rykaczewski, M. Wolińska-Cichocka, K. C. Goetz, R. K. Grzywacz, C. J. Gross, K. Miernik, and S. V. Paulauskas, Journal of the Physical Society of Japan Conference Proceedings **6**, 030018 (2015).

[54] T. Kibédi, T. W. Burrows, M. B. Trzhaskovskaya, P. M. Davidson, and C. W. Nestor, Nuclear Instruments and Methods in Physics Research Section A: Accelerators, Spectrometers, Detectors and Associated Equipment **589**, 202 (2008).

[55] F. Bečvář, Nuclear Instruments and Methods in Physics Research Section A: Accelerators, Spectrometers, Detectors and Associated Equipment **417**, 434 (1998).

[56] J. L. Tain and D. Cano-Ott, Nuclear Instruments and Methods in Physics Research Section A: Accelerators, Spectrometers, Detectors and Associated Equipment **571**, 719 (2007).

[57] D. Jordan, A. Algora, and J. L. Tain, Nuclear Instruments and Methods in Physics Research Section A: Accelerators, Spectrometers, Detectors and Associated Equipment **828**, 52 (2016).

[58] D. Pandit, S. Bhattacharya, D. Mondal, P. Roy, K. Banerjee, S. Mukhopadhyay, S. Pal, A. De, B. Dey, and S. R. Banerjee, Phys. Rev. C **97**, 041301 (2018).

[59] S. Bhattacharya, D. Pandit, S. Mukhopadhyay, S. Pal, and S. R. Banerjee, Phys. Rev. C **78**, 064601 (2008).

[60] S. Bhattacharya, D. Pandit, B. Dey, D. Mondal, S. Mukhopadhyay, S. Pal, A. De, and S. R. Banerjee,

Phys. Rev. C **90**, 054319 (2014).
[61] F. Pühlhofer, Nuclear Physics A **280**, 267 (1977).
[62] G. Schramm, R. Massarczyk, A. R. Junghans, T. Belgya, R. Beyer, E. Birgersson, E. Grosse, M. Kempe, Z. Kis, K. Kosev, M. Krtička, A. Matic, K. D. Schilling, R. Schwengner, L. Szentmiklósi, A. Wagner, and J. L. Weil, Phys. Rev. C **85**, 014311 (2012).
[63] L. E. Kirsch and L. A. Bernstein, Nuclear Instruments and Methods in Physics Research Section A: Accelerators, Spectrometers, Detectors and Associated Equipment **892**, 30 (2018).
[64] S. Goriely, S. Hilaire, and A. J. Koning, Phys. Rev. C **78**, 064307 (2008).
[65] T. Kurtukian-Nieto, J. Benlliure, and K.-H. Schmidt, Nuclear Instruments and Methods in Physics Research Section A: Accelerators, Spectrometers, Detectors and Associated Equipment **589**, 472 (2008).
[66] A. C. Dombos, D.-L. Fang, A. Spyrou, S. J. Quinn, A. Simon, B. A. Brown, K. Cooper, A. E. Gehring, S. N. Liddick, D. J. Morrissey, F. Naqvi, C. S. Sumithrarachchi, and R. G. T. Zegers, Phys. Rev. C **93**, 064317 (2016).
[67] J. C. Hardy and I. S. Towner, Phys. Rev. C **79**, 055502 (2009).
[68] J. C. Hardy and I. S. Towner, Nuclear Physics News **16**, 11 (2006).
[69] J. Blachot, Nuclear Data Sheets **83**, 1 (1998).
[70] B. Singh and Z. Hu, Nuclear Data Sheets **98**, 335 (2003).
[71] H. Bateman, Proceedings of the Cambridge Philosophical Society **15**, 423 (1910).
[72] Meng Wang, G. Audi, F. G. Kondev, W. J. Huang, S. Naimi, and Xing Xu, Chinese Physics C **41**, 030003 (2017).
[73] M. Graefenstedt, U. Keyser, F. Münnich, F. Schreiber, H. R. Faust, and H. Weikard, Zeitschrift für Physik A Atomic Nuclei **327**, 383 (1987).
[74] H. Ohm, M. Liang, U. Paffrath, B. De Sutter, K. Sistemich, A. -M. Schmitt, N. Kaffrell, N. Trautmann, T. Seo, K. Shizuma, G. Molnár, K. Kawade, and R. A. Meyer, Zeitschrift für Physik A Hadrons and Nuclei **340**, 5 (1991).
[75] E. Browne and J. K. Tuli, Nuclear Data Sheets **145**, 25 (2017).
[76] S. Rinta-Antila, T. Eronen, V.-V. Elomaa, U. Hager, J. Hakala, A. Jokinen, P. Karvonen, H. Penttilä, J. Rissanen, T. Sonoda, A. Saastamoinen, and J. Äystö, The European Physical Journal A **31**, 1 (2007).
[77] D. De Frenne, Nuclear Data Sheets **110**, 1745 (2009).
[78] V. Guadilla, A. Algora, J. L. Tain, M. Estienne, M. Fallot, A. A. Sonzogni, J. Agramunt, J. Äystö, J. A. Briz, A. Cucoanes, T. Eronen, L. M. Fraile, E. Ganioğlu, W. Gelletly, D. Gorelov, J. Hakala, A. Jokinen, D. Jordan, A. Kankainen, V. Kolhinen, J. Koponen, M. Lebois, L. Le Meur, T. Martinez, M. Monserrate, A. Montaner-Pizá, I. Moore, E. Nácher, S. E. A. Orrigo, H. Penttilä, I. Pohjalainen, A. Porta, J. Reinikainen, M. Reponen, S. Rinta-Antila, B. Rubio, K. Rytkönen, T. Shiba, V. Sonnenschein, E. Valencia, V. Vedia, A. Voss, J. N. Wilson, and A.-A. Zakari-Issoufou, Phys. Rev. Lett. **122**, 042502 (2019).
[79] V. G. Gómez, *TAGS measurements for neutrino physics and applications*, Ph.D. thesis, The University of Valencia (2017).
[80] V. Guadilla, J. L. Tain, A. Algora, J. Agramunt, J. Äystö, J. A. Briz, A. Cucoanes, T. Eronen, M. Estienne, M. Fallot, L. M. Fraile, E. Ganioğlu, W. Gelletly, D. Gorelov, J. Hakala, A. Jokinen, D. Jordan, A. Kankainen, V. Kolhinen, J. Koponen, M. Lebois, L. Le Meur, T. Martinez, M. Monserrate, A. Montaner-Pizá, I. Moore, E. Nácher, S. E. A. Orrigo, H. Penttilä, I. Pohjalainen, A. Porta, J. Reinikainen, M. Reponen, S. Rice, S. Rinta-Antila, B. Rubio, K. Rytkönen, T. Shiba, V. Sonnenschein, A. A. Sonzogni, E. Valencia, V. Vedia, A. Voss, J. N. Wilson, and A.-A. Zakari-Issoufou, Nuclear Instruments and Methods in Physics Research Section A: Accelerators, Spectrometers, Detectors and Associated Equipment **910**, 79 (2018).
[81] S. Kumar, J. Chen, and F. G. Kondev, Nuclear Data Sheets **137**, 1 (2016).
[82] D. D. Frenne and A. Negret, Nuclear Data Sheets **109**, 943 (2008).
[83] T. Mehren, B. Pfeiffer, S. Schoedder, K.-L. Kratz, M. Huhta, P. Dendooven, A. Honkanen, G. Lhersonneau, M. Oinonen, J.-M. Parmonen, H. Penttilä, A. Popov, V. Rubchenya, and J. Äystö, Phys. Rev. Lett. **77**, 458 (1996).
[84] J. Pereira, S. Hennrich, A. Aprahamian, O. Arndt, A. Becerril, T. Elliot, A. Estrade, D. Galaviz, R. Kessler, K.-L. Kratz, G. Lorusso, P. F. Mantica, M. Matos, P. Möller, F. Montes, B. Pfeiffer, H. Schatz, F. Schertz, L. Schnorrenberger, E. Smith, A. Stolz, M. Quinn, W. B. Walters, and A. Wöhr, Phys. Rev. C **79**, 035806 (2009).
[85] M. K. Smith, *Chasing Triaxiality: Probing Structure in the $A \sim 110$ Region via Lifetime Measurements of 109Ru and 109Tc with Fast Timing*, Ph.D. thesis, University of Notre Dame (2017).
[86] J. Kurpeta, W. Urban, A. Płochocki, J. Rissanen, J. A. Pinston, V.-V. Elomaa, T. Eronen, J. Hakala, A. Jokinen, A. Kankainen, I. D. Moore, H. Penttilä, A. Saastamoinen, C. Weber, and J. Äystö, Phys. Rev. C **86**, 044306 (2012).
[87] H. Penttilä, *Studies of Very Neutron-Rich Odd-Mass Nuclei with $109 \leq A \leq 119$*, Ph.D. thesis, University of Jyväskylä (1992).
[88] P. Möller, R. Bengtsson, B. G. Carlsson, P. Olivius, and T. Ichikawa, Phys. Rev. Lett. **97**, 162502 (2006).
[89] P. Möller, R. Bengtsson, B. G. Carlsson, P. Olivius, T. Ichikawa, H. Sagawa, and A. Iwamoto, Atomic Data and Nuclear Data Tables **94**, 758 (2008).
[90] P. Möller, A. J. Sierk, R. Bengtsson, H. Sagawa, and T. Ichikawa, Atomic Data and Nuclear Data Tables **98**, 149 (2012).
[91] E. Chabanat, P. Bonche, P. Haensel, J. Meyer, and R. Schaeffer, Nuclear Physics A **635**, 231 (1998).
[92] J. Kurpeta, W. Urban, A. Płochocki, J. Rissanen, J. A. Pinston, V.-V. Elomaa, T. Eronen, J. Hakala, A. Jokinen, A. Kankainen, P. Karvonen, I. D. Moore, H. Penttilä, A. Saastamoinen, C. Weber, and J. Äystö, Phys. Rev. C **84**, 044304 (2011).
[93] T. Marketin, D. Vretenar, and P. Ring, Phys. Rev. C **75**, 024304 (2007).
[94] T. Marketin, L. Huther, and G. Martínez-Pinedo, Phys. Rev. C **93**, 025805 (2016).
[95] P. Möller and J. Randrup, Nuclear Physics A **514**, 1 (1990).

[96] P. Möller, M. R. Mumpower, T. Kawano, and W. D. Myers, Atomic Data and Nuclear Data Tables **125**, 1 (2019).